WESTFÄLISCHE WILHELMS-UNIVERSITÄT MÜNSTER

MASTER THESIS

Replication of a photomultiplier in COMSOL Multiphysics® to study PMT performance parameters for the mDOM in IceCube

---

Supervisor:
Prof. Dr. Alexander KAPPES

Second examiner:
Prof. Dr. Christian WEINHEIMER

A thesis submitted in the fulfilment of the requirements for the degree of
Master of Science *at* Westfälische Wilhelms-Universität Münster

by

Willem ACHTERMANN

AG Kappes
Institute for Nuclear Physics
Department of Physics

Monday 18th September, 2023

Contents

1 Introduction

The detection of light plays an important role our everyday life as well as science. From microscopes in biology and medicine to telescopes in astronomy, photons are the prominent messenger carrying the desired information. In astronomy, this results in stunning images of the night sky where the ability to detect light goes far beyond the visible spectrum out eyes are limited to.

Enter, neutrinos. First postulated by W. Pauli in 1930 when observing the energy spectrum of electrons from the β-decay [1] and detected in 1956 by C.L. Cowan and F. Reines in the poltergeist-experiment [2], it is one of the most abundant particles in the known universe but largely unknown to the general public. With an exceptionally small interaction cross section due to only interacting through the weak interaction and negligibly contributions from gravity, neutrinos propagate through the universe on straight paths. This characteristic makes neutrinos interesting for astronomy as their origin may lie in distant objects and is connected to the acceleration sites of cosmic rays.

The IceCube Neutrino Observatory [3] is dedicated to the detection of neutrinos. It utilises an indirect method where the neutrino first interacts with matter. The emerging particles are subsequently detected via the Cherenkov effect [4] which describes the emission of light from charged particles traveling in a dielectric medium. The underlying mechanisms to this detection method are outlined in chapter 2. In IceCube, a $\sim 1\,\mathrm{km}^3$ portion of the glacial ice in the south pole is used as the detection medium to increase the probability of the neutrino interaction. The ice is fitted with over 5000 modules responsible to detect the light stemming from the neutrino interaction. At the heart of each of these modules is a photomultiplier tube (PMT). Currently, two extensions for the existing detector are planned. IceCube Upgrade [5] and IceCube-Gen2 [6] in which new optical modules will be deployed among other improvements. One of these modules is the multi PMT digital optical module, or mDOM, utilizing 24 PMTs of $80\,\mathrm{mm}$ diameter. This thesis focuses on these PMTs and the principle and properties of them are explained (see chapter 3) as well as explored. PMTs are the main components of modern neutrino telescopes and the knowledge of their characteristics directly influences the operation of such telescopes. In this thesis, two aspects are studied. The collection efficiency and the timing properties.

The studies are conducted in a simulation software called COMSOL Multiphysics® which is widely used in science to model physics, chemistry or engineering processes. The important aspects of the software for the purpose of the PMT simulation are highlighted in chapter 4, while chapter 5 explores the accuracy of the simulation.

The analysis of the simulated data and comparison to measurement data of actual mDOM PMTs is presented in chapter 6 for two different photocathode illumination patterns. A combination of these patterns is used in chapter 7 to explore the photosensitive area of the PMT in two dimensions.

2 Astronomy with neutrinos

This chapter gives a brief introduction to neutrino physics (see section 2.1) and highlights its importance in multi messenger astronomy (see section 2.2). In section 2.3 the Cherenkov radiation is introduced, which is used in the IceCube Neutrino Observatory outlined in section 2.4. Finally, section 2.5 broaches the extensions of this detector.

2.1 Neutrinos in the standard model

Neutrinos are one of the most abundant particles in the universe and yet they rarely interact with matter. This is due to their unique properties. Neutrinos are particles in the standard model of particle physics shown in figure 2.1.1 and come in three generations, also called flavours. Namely the electron-neutrino ν_e, the muon-neutrino ν_μ and the tau-neutrino ν_τ.

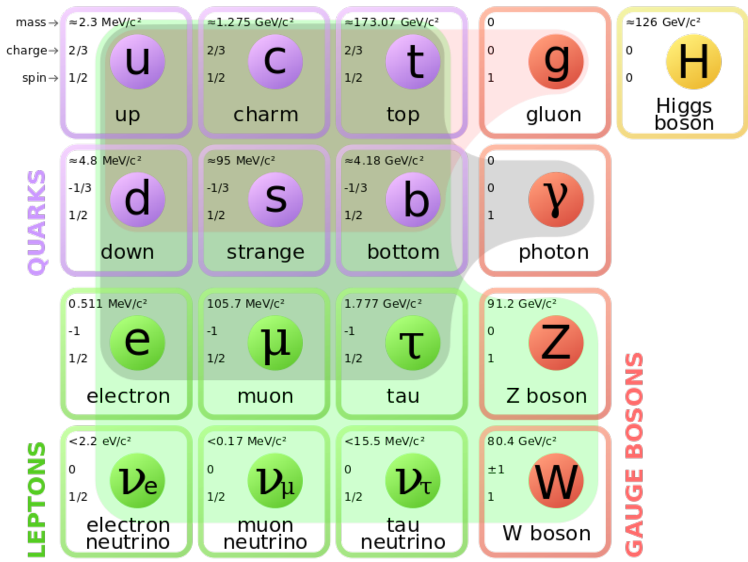

Figure 2.1.1: The standard model of particle physics with mass, charge and spin of the particles. The color indicates the possible interactions of the particles (red: strong, grey: electromagnetic, green: weak). Image taken from [7].

As fermions, the neutrinos posses a spin of $1/2$ and further belong to the leptons. Since the neutrino does not carry an electrical or color charge and its mass is exceptionally small it only interacts through the weak interaction. The short range of the weak interaction is also the reason for the low rate of interaction between a neutrino and matter. The weak interaction is split into the **neutral current** (NC) and **charged current** (CC) depending on the exchanged boson. For the energy regime of interest an interaction usually occurs through deep inelastic scattering. The possible interactions are then given by

$$\overset{(-)}{\nu_l} + N \xrightarrow{Z^0} \overset{(-)}{\nu_l} + X \quad \text{(NC)} \tag{2.1.1}$$

$$\overset{(-)}{\nu_l} + N \xrightarrow{W^\pm} l^\mp + X \quad \text{(CC)}, \tag{2.1.2}$$

where $l \in \{e, \mu, \tau\}$ denotes the flavour of the neutrino and lepton, N is a nucleon and X represents further hadronic products.

For a long time it was believed that neutrinos do not have a mass. This believe, however, changed when the phenomenon of **neutrino oscillation** was observed [8] [1] whereby the flavor of a neutrino changes when it propagates through matter. This lead to the conclusion that the neutrino flavours propagate as a mixture of mass eigenstates. These mass eigenstates propagate at different speeds resulting in the flavour oscillation. This effect is only possible if the difference between the mass eigenstates is non zero. Therefore, the neutrinos must have a mass. The absolute value of this mass remains a mystery to this day as there are only upper limits known through various experiments like the KATRIN experiment [9] currently limiting the neutrino mass to $m_\nu \leq 0.8\,\mathrm{eV}$ [10].

2.2 Neutrino sources

Neutrinos can originate from several sources. On earth, they are produced, for example, in nuclear reactors, through the β-decay of radioactive isotopes, and as a product of cosmic ray showers.[2] Additionally, there is an extraterrestrial component contributing to the overall neutrino flux that is measured. The different sources and their fluxes are shown in figure 2.2.1.

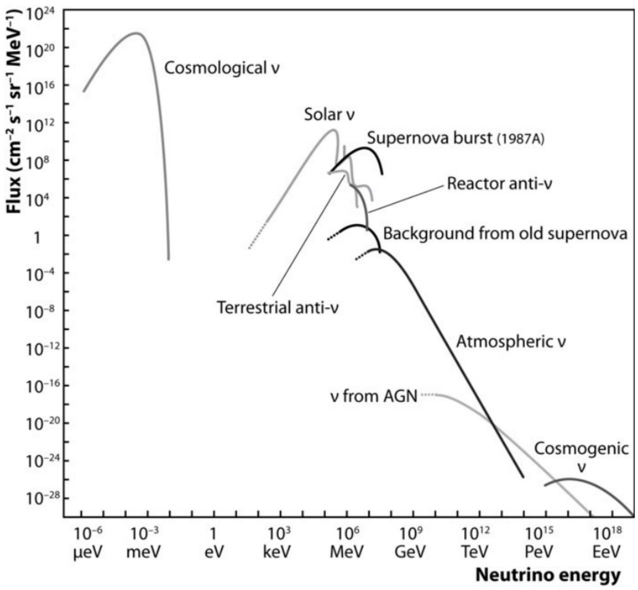

Figure 2.2.1: Neutrino fluxes from different sources. Shown are both measured and theoretical fluxes. Image taken from [12].

Most of the extraterrestrial neutrinos that reach earth originate from our sun. They are produced in nuclear fusion processes where hydrogen nuclei are converted to helium. Due to their low interaction rate they can then escape the sun and propagate towards the earth.

Of interest for astronomy are neutrinos that have their origin outside of our solar system in astrophysical objects like supernovae and active galactic nuclei (AGN). Traditional telescopes are very capable when it comes to finding and observing these objects but they only focus on the electromagnetic spectrum. This is limited due to the possible scattering

[1]This resulted in the nobel price for Takaaki Kajita and Arthur B. McDonald in 2015.
[2]Cosmic rays are ionized nuclei with very high energies up to 10^{20}eV [11].

of its messenger, the photon. The unique properties of the neutrino, namely only interacting weakly, results in them taking a direct path from their point of origin and detection. By observing the path of a neutrino one can therefore point directly to its source. They are a complementary messenger to the photon. This principle of observing multiple messengers lead to the suggestion that blazars [3] are a source of high energy astrophysical neutrinos when one such neutrino was observed in 2017 by the IceCube Neutrino Observatory from the TXS $0506 + 056$ blazar. This happened coincidentally with a γ-ray flare [13]. This suggestion was later strengthened when archival data was reinvestigated and an excess of high energy neutrino events was found in the direction of the blazar [14].

Further searches in previously recorded data where the positions of known γ-ray sources were investigated for an overabundance of neutrinos above expectations were performed. These searches provide evidence that the active galaxy NGC 1068 is emitting neutrinos in the TeV range [15]. Most recently the investigation of archival data with a new machine learning based approach show that the galactic plane of the milky way is a source of neutrinos with $4.5\,\sigma$ confidence [16].

2.3 Cherenkov radiation

As discussed previously, when a neutrino interacts with matter there is the possibility of generating charged particles. When these charged particles have sufficient energy and traverse trough a dielectric medium they induce what is referred to as Cherenkov radiation [4].

While the speed of light in vacuum c_0 is an absolute constant in physics, light propagates at different speeds depending on the medium. This propagation speed is determined by the refractive index n of the medium. One can then calculate the speed of light in the medium using $c_n = c_0/n$.

When a charged particle travels through a dielectric medium, it polarises the surrounding particles of the medium. By radiating photons these particles will return to their original state. If the charged particle is slower than the speed of light in that medium, the emitted photons will interfere destructively. Should the charged particle be faster than the speed of light in the medium, the emitted light will interfere constructively resulting in a cone shaped waveform along the propagation direction of the charged particle like shown in figure 2.3.1.

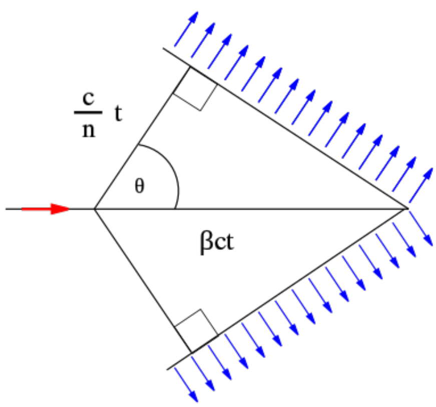

Figure 2.3.1: Representation of the Cherenkov effect. Shown is the incoming charged particle (red) and the resulting radiation (blue) with angle θ to the direction of propagation. Image taken from [17].

[3] A blazar is a AGN with the jet pointed towards the earth.

Here the incoming particle (red arrow) will result in the emission of Cherenkov radiation (blue arrows) along its trajectory. The angle at which the light is emitted depends on the speed of the charged particle and the refractive index of the medium. In a time t the charged particle will travel the distance vt and the light ct/n. Using the cosine law for right triangles one can calculate the angle to be determined by

$$\cos\theta = \frac{1}{\beta \cdot n}, \tag{2.3.1}$$

where $\beta = v/c_0$ denotes the ratio between the speed of the particle and the speed of light in vacuum. The Cherenkov effect is widely used in a multitude of experiments around the world. The application in the IceCube experiment shall now be discussed.

2.4 The IceCube Neutrino Observatory

The neutrino is truly a double edged sword when it comes to astronomy as it provides a new point of view but also pose challenges to be able to utilize its potential. Due to their unchanged trajectory neutrinos are an ideal messenger and considered to be a "smoking gun" for the production of cosmic rays. However, this property also means that the amount of neutrinos one can detect from the objects in question is small.

One instrument that takes advantage of neutrinos is the IceCube Neutrino Observatory [3], or shorter, IceCube. It is located at the South Pole and uses an array of optical modules to detect the radiation that occurs after a neutrino interaction. A sketch of the experiment is depicted in figure 2.4.1.

IceCube uses a total of 86 strings that are embedded in the polar ice at depths between $1450\,\mathrm{m}$ and $2450\,\mathrm{m}$. The layout of the strings follows an approximate hexagonal grid with spacing between two strings of up to $125\,\mathrm{m}$. The strings themselves consist of multiple digital optical modules (DOMs) that are used to detect the light produced after neutrino interactions. The total instrumented volume of the detector amounts to about $1\,\mathrm{km}^3$ which can be split into three major parts as follows:

- The **In-Ice** array is the largest part of the detector and the most prominent one as well. It is built with 78 of the 86 strings, populated with 60 DOMs each. The vertical distance between modules is $\sim 17\,\mathrm{m}$ resulting in a design that is optimized for the TeV to PeV energy range. In figure 2.4.1 the In-Ice array is shown in blue.

- The **DeepCore** array is the set of the remaining eight strings but also utilizes seven neighbouring stings from the In-Ice array. The DeepCore strings also contain 60 DOMs each. 50 of these modules are located at depths below $2100\,\mathrm{m}$ and 10 shallower than $2000\,\mathrm{m}$. This way the dustlayer [4] can be avoided. The spacing between the DOMs is $7\,\mathrm{m}$ and $10\,\mathrm{m}$ for the lower and upper part respectively. This tighter geometry is chosen to enhance the sensitivity for lower energies down to $10\,\mathrm{GeV}$. The DeepCore array is colored green in figure 2.4.1.

- The **IceTop** surface array is located on the surface as the name implies. It adds another 324 DOMs contained in 81 stations to the detector. IceTop is used to observe cosmic ray showers but can also be used as a veto for downgoing muons.

The most important part of the detector is the DOM. It essentially is the interface between the neutrino and the measurement. The main components of a DOM can be seen in figure 2.4.2.

[4]The dustlayer is a region of poor optical quality inside the ice.

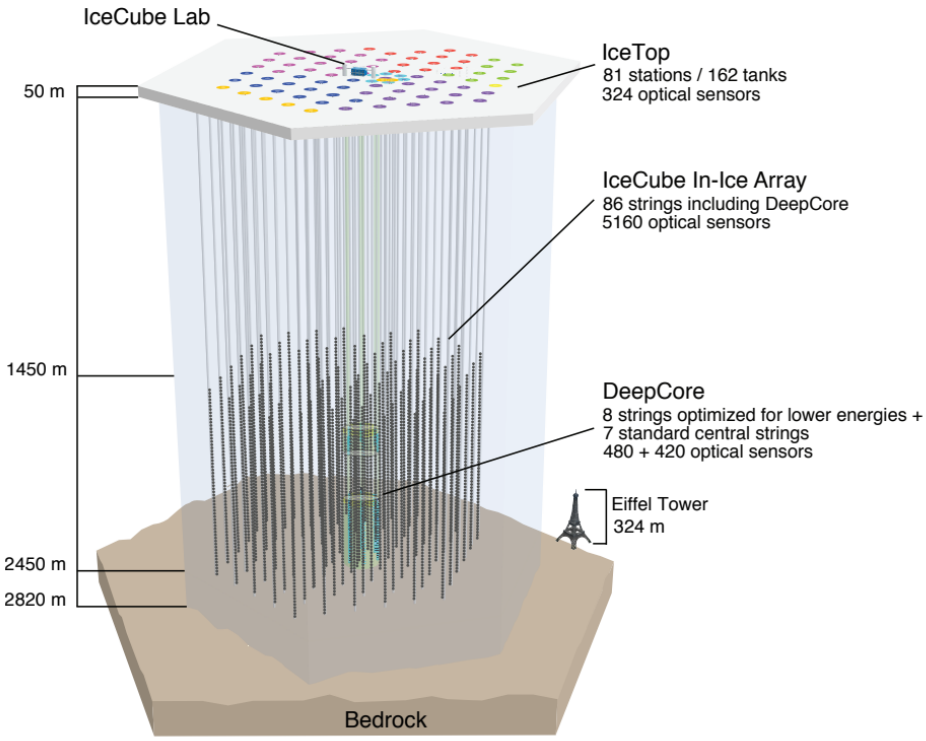

Figure 2.4.1: Schematic drawing of the IceCube Neutrino Observatory. Shown are the In-Ice array (blue), the DeepCore array (green), the IceTop surface array and the scale of the detector. The colors on top indicate the different deployment seasons. Image taken from [18].

At the heart of every DOM is a photomultiplier tube (PMT) of 24 cm diameter. These devices are used to convert light into an electrical signal and are described in more detail in chapter 3. The DOM also contains the necessary electronics to operate the PMT as well as calibration devices. All of these components are housed inside a glass pressure vessel protecting them from environmental conditions (not shown in figure 2.4.2) and then lowered into the ice.

The information one hopes to obtain from operating the detector is an accurate value for the energy and direction of the incoming particles. What the detector actually sees, however, are only photons that can originate from said particles. The data acquired by the DOMs contains the detected charge [5] over time. With this information and appropriate reconstruction algorithms, one can estimate the energy and direction of the incoming particles. Depending on the type of particle/neutrino interaction there are two different major signatures coming from two event types [6], namely the cascade (sometimes called shower) shown in figure 2.4.3a and track seen in figure 2.4.3b.

Track signatures are only caused by muons. They can either be generated by CC ν_μ interactions or in the atmosphere. Due to the greater mass of the muon it can travel further inside of the detector and deposit its energy along its path. The reconstruction of the muon energy is difficult for the track signature since parts of the track lie outside the detector. The direction, however, can be reconstructed with degree-precision and better depending on the energy [20]. This makes tracks the optimal signature for finding point-sources.

[5] This is related to the number of photons arriving at the DOM

[6] There is a third event type called "double-bang" which is a combination of two showers connected by a track. It can only come from ν_τ which have not been detected yet.

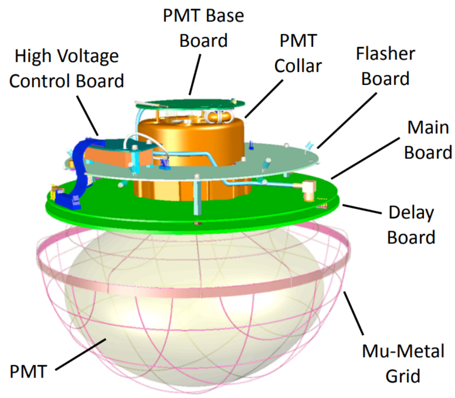

Figure 2.4.2: Mechanical layout of the DOM consisting of PMT, calibration devices, readout electronics and high voltage supply. The glass pressure vessel is not shown. Image taken from [18].

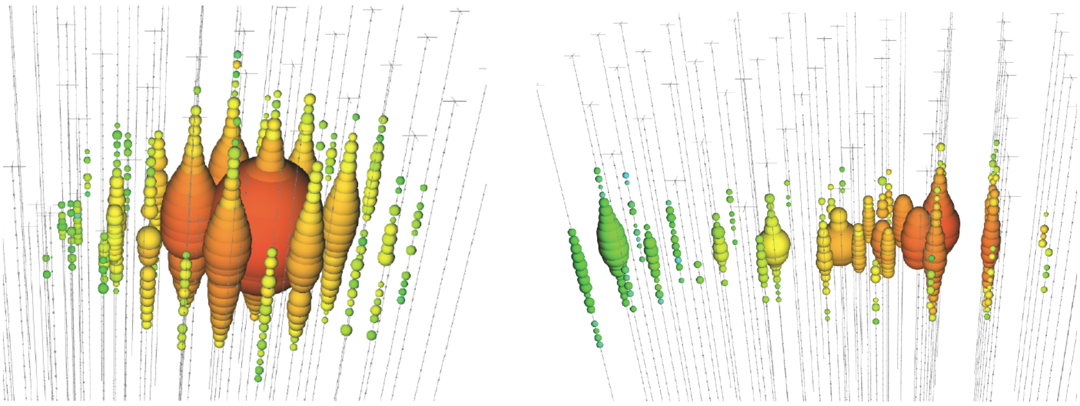

(a) Shower event **(b)** Track event

Figure 2.4.3: Two different event signatures in the IceCube detector. Figure 2.4.3a shows the signature of shower events and figure 2.4.3b that of track events. Images taken from [19], modified.

All NC interactions will result in a cascade event together with ν_e CC interactions. The produced electrons travel much shorter distances inside the detector and deposit their energy rapidly. This leads to an almost spherical shape of the signal. Apart from this there is also the hadronic cascade from NC [7] interactions. They share the same signature. Since most of the energy is deposited and detected inside of the detector the reconstruction of the energy is superior to that of track events. The directional reconstruction is limited in its accuracy due to the spherical shape of the signal.

2.5 IceCube Upgrade and the mDOM

Two future IceCube extensions are planned, aiming to improve the already impressive capabilities of the existing detector and to further enhance it's sensitivity for lower and higher energies. One is IceCube-Gen2 [6] where the instrumented volume will be increased significantly allowing the detection of higher energy events in the TeV to EeV range [21]. The other is called IceCube Upgrade [5] which will lower the energy threshold to a few GeV and provide new calibration methods for the existing detector [5]. The future layout of the current detector including IceCube Upgrade is shown in figure 2.5.1a. In total seven new strings with

[7] Hadronic cascades also happen with CC interactions.

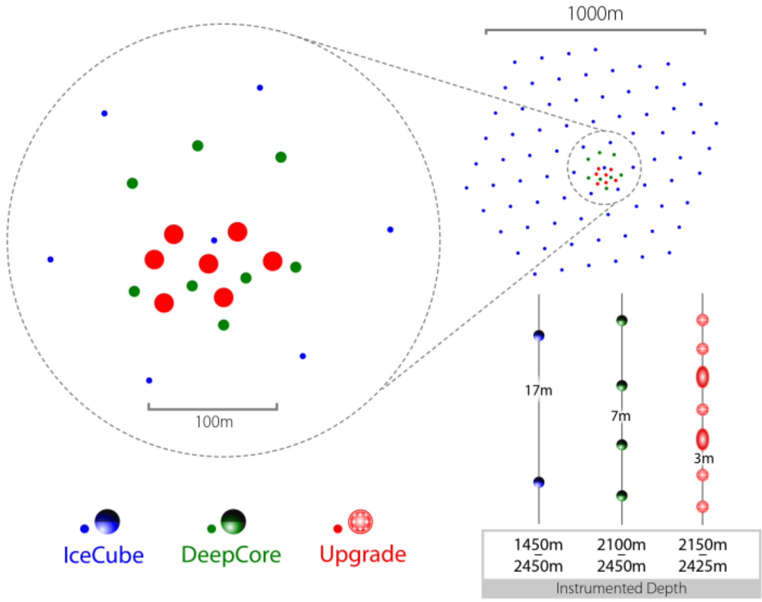

(a) Layout of IceCube Upgrade.

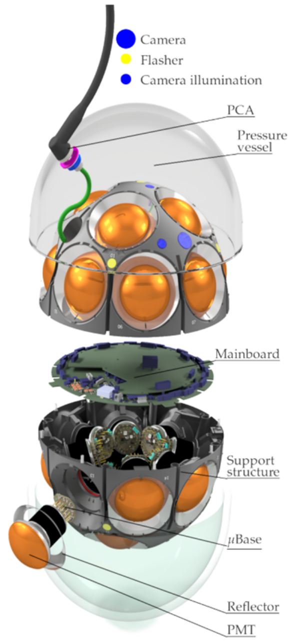

(b) Exploded view of an mDOM.

Figure 2.5.1: Planned layout for the IceCube Upgrade detector in figure 2.5.1a and exploded view of the mDOM in figure 2.5.1b. Images taken from [5] and [22], respectively.

approximately 700 newly developed optical modules will be deployed. The deployment of the IceCube Upgrade stings is planned for 2025/26.

One of these optical modules is the multi-PMT digital optical module, or mDOM, depicted in figure 2.5.1b. It houses a total of 24 PMTs of 80 mm diameter including their electronics and several calibration devices inside. This segmented approach has several advantages over the previous DOM such as a larger sensitive area with near 4π coverage and inherent directional information about incoming photons. There has been a lot of research into this module and the knowledge gained will be used to construct the module for IceCube-Gen2. This thesis is focused on the PMT used in the mDOM.

3 Photomultiplier tubes

Photomultiplier Tubes (PMTs) are a widely used instrument for the detection of light in different fields of physics, biology, chemistry or medicine. They are also the main component of the IceCube detector as mentioned in section 2.4. This chapter will give an overview of the working principles of PMTs in section 3.1 with the discussion of their properties relevant to this thesis in section 3.2. The theory of the photoelectric effect and secondary emission in this context are explained as well in section 3.3 and section 3.4 respectively.

3.1 PMT working principle

The working principle of a PMT can be explained in three steps. The first step is the conversion of a photon to an electron. This takes place at the photocathode, a thin layer of photosensitive material. If the photon is absorbed it can liberate an electron, called photoelectron. This step (further discussed in section 3.3) is followed by a multiplication process, consisting of a series of stages (called dynodes) where the photoelectron is accelerated due to a step-wise increasing electric potential inside the PMT. When striking a dynode, the photoelectron releases secondary electrons from the dynode material. These are then accelerated towards the next dynode where further electrons are liberated. This is repeated multiple times until a certain amount of electrons is accumulated. Finally, the combined charge of all the electrons is collected and measured at the anode. The total number of collected electrons can differ depending on the application but is usually in the order of 10^6 to 10^7. The schematics of the described process as well as the essential component housed in a vacuum inside a glass bulb are shown in figure 3.1.1.

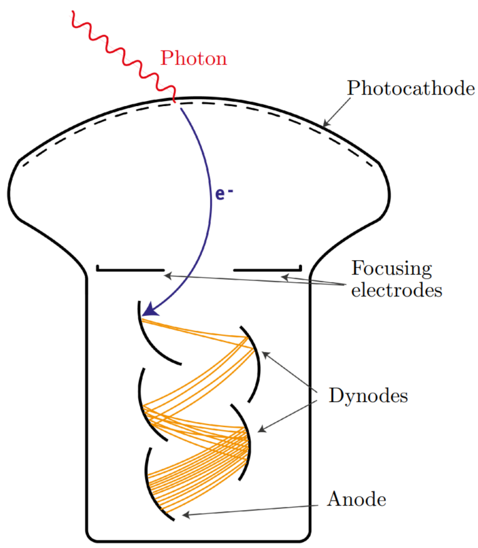

Figure 3.1.1: Schematic drawing of a PMT with the main components. The incoming photon (red) frees an electron from the photocathode (dashed line) which is accelerated towards the dynodes and successively multiplied (orange). The combined charge is collected at the anode. Image taken from [23].

As mentioned above there is an electric field inside the PMT. This is generated with a high voltage power supply. The potential is then divided onto the different components. The IceCube mDOM PMT [8] has a total of ten dynodes. The important metric for the multiplication process is the potential difference between the stages (further discussed in section 3.4). In case of the mDOM PMT the first dynode gets the largest share of $3/13$th while the rest of the components only get $1/13$th of the total electric potential applied. Note that the anode also needs a share of the total potential but does no further multiplication.

3.2 PMT properties

A PMT has numerous properties that impact its performance. This section will give an overview of some of these properties, which are relevant to this thesis. The dependencies of these properties on some parameters are also discussed.

3.2.1 Gain and collection efficiency

The gain of a PMT determines how many electrons are collected on average at the anode when one photoelectron is emitted from the photocathode. It is the product of the gain of each multiplication stage and can be written as

$$g = \prod \delta_i \cdot c_i, \tag{3.2.1}$$

where δ_i is the secondary emission yield and c_i is the collection efficiency of dynode i. The secondary emission yield δ is a material property and will be further examined in section 3.4. It describes the average number of new electrons liberated from the dynode per incident electron. The collection efficiency c is the ratio between the number of emitted electrons at the previous stage to the number of electrons arriving. The gain of a PMT can be adjusted by changing the supply voltage like shown in figure 3.2.1.

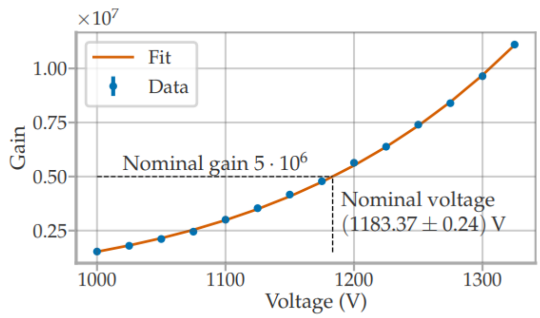

Figure 3.2.1: Measured gain of an IceCube mDOM PMT against the supplied voltage. The necessary voltage to achieve nominal gain of $5 \cdot 10^6$ is extracted from a fit. Image taken from [22], modified.

This is explained by the dependence of the secondary emission yield on the energy of the incoming particles and therefore on the supply voltage. This is by far the easiest way to change the gain of the PMT as otherwise the dynode material would need to be changed to increase the secondary emission yield or the geometry changed to increase the collection efficiency. It is important to note that the collection efficiency of the first stages influences the gain to a higher degree than latter stages since the "lost" electrons wont get multiplied.

The characterization of PMTs is typically done at their nominal gain which is $5 \cdot 10^6$ for the mDOM PMT. The voltage necessary to achieve this varies between PMTs, though.

[8] Model: Hamamatsu R15458

3.2.2 Timing parameters

Of particular interest for the IceCube experiment is the timing performance of the PMTs since in the reconstruction of events the arrival time of the photons plays a central role. There are two separate categories of timing parameters. The first are concerned with the properties of a single PMT pulse and the second with the difference between pulses. A single pulse for a PMT is depicted in figure 3.2.2a.

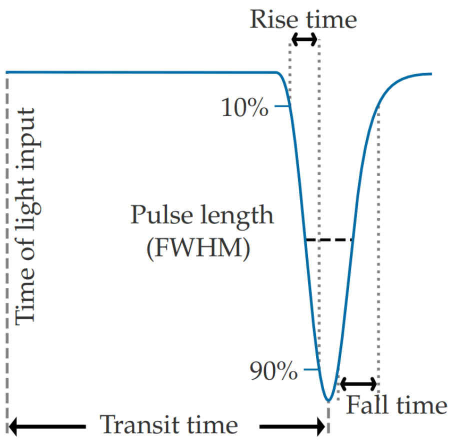

(a) Single pulse

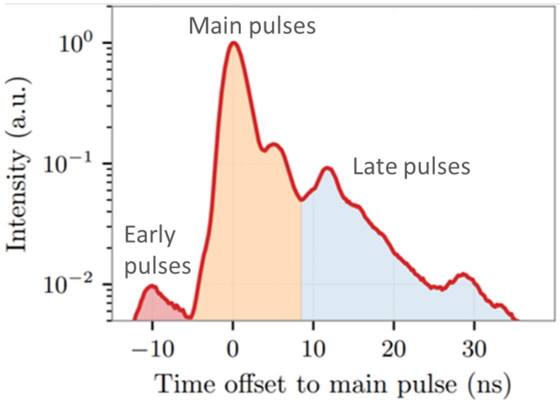

(b) Pulse distribution

Figure 3.2.2: Theoretical shape of the pulse of a PMT in figure 3.2.2a with the transit time, rise time, fall time and pulse length. Image taken from [22]. When putting the transit time of multiple pulses into a histogram the three regions in figure 3.2.2b are obtained. The main pulse (orange), early pulses (red) and late pulses (blue) are shown. Image taken from [24], modified.

It has a transit time (TT) which is the time difference between the light hitting the photocathode and the signal being measured at the anode. The shape of the pulse is described by the rise and fall time. This is the time interval in which the signal rises from 10 % to 90 % or vise versa. The length of the pulse is determined by the FWHM of the signal.

The transit time of a PMT is not a constant value. If the transit times of several pulses are grouped in a histogram a distribution similar to that in figure 3.2.2b will appear which can be divided into three regions.

The first region describes the early pulses. These are photons that are transmitted through the photocathode and hit the first dynode. Here an electron is liberated from the material and multiplied. Since this pulse is missing the first stage of amplification it has a lower gain and therefore is harder to detect. The photon is much faster than the electron so this type of pulse appears earlier than expected with the time difference depending on the PMT geometry.

The second group of pulses are all close to the maximum of the distribution. They are categorized as main pulses and most of them are generated by the ordinary method. They have a spread, called transit time spread (TTS), which can come from different trajectories or starting positions of the photoelectron.[9]

Lastly there are pulses that arrive after the main pulse. An electron can elastically scatter on the first dynode.[10] This results in a longer trajectory inside the PMT resulting in a delayed detection of a few ns. Another possibility is the so-called afterpulsing. Here the impact of the electron causes the generation of a photon which can trigger a second pulse when it hits

[9] One of the goals of this thesis is to better understand this feature.

[10] This is also possible on the other dynodes but the effect is most noticeable for the first, due to the absence of other secondary electrons.

the photocathode. Additionally, electrons can ionize residual atoms in the PMT vacuum. These positive charged ions are accelerated towards the photocathode and liberate a large number of electrons which trigger pulses. Both types of afterpulses are considered correlated background of the PMT and follow after the main pulse while late pulses replace it.

3.3 Photoelectric effect

This section will focus on the photoelectric effect. This in general describes the emission of electrons from materials when illuminated with light of sufficient energy. As this is a very broad topic, this section will only focus on the photoemission from the photocathode type used in the IceCube mDOM PMT. These are made out of a bialkali material [25] the exact constituents of which are unknown and classify as a semiconductor. The process of photoemission can be split into three parts depicted in figure 3.3.1, often referred to as the Three Step Model [26].

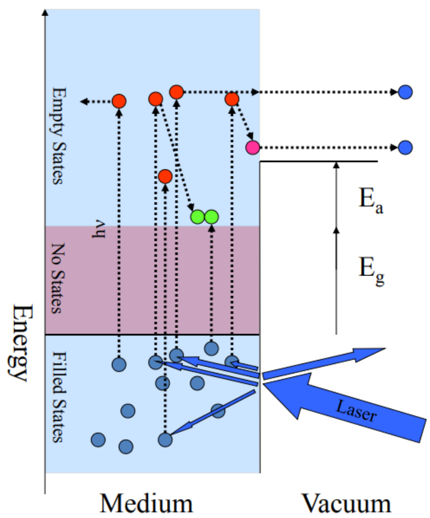

Figure 3.3.1: Three step model for photoemission. First the light is absorbed in the medium and elevates electrons from filled states to empty states. The electron needs to transit to the surface of the material in a random walk and then overcome the electron affinity to escape into the vacuum. Image taken from [27], modified.

1. The first step is the **excitation of an electron** from the valence band into the conduction band. This step is governed by the optical properties of the material since light can get either reflected, transmitted or absorbed. In semiconductors there is a band gap with a width of E_g where no electrons can be situated. The photon needs to have at least this much energy to promote the electron. The absorption probability of a photon further depends on the thickness of the material. The electrons will have an energy distribution before the excitation which is described by the Fermi-Dirac statistic combined with the density of states of the material [28].

2. The excited electron needs to **transit to the surface** of the material. During this process the electron can undergo multiple scattering processes with the lattice of the material [11] resulting in a loss of energy. In total the movement of the electron can be described as a random walk.

[11] Scattering with electrons is also possible but highly unlikely since the conduction band of a semiconductor is almost empty [29].

3. In order to **escape from the surface** the electron needs to have more energy than the electron affinity (denoted E_a in figure 3.3.1) of the material.

The final distributions for the energy and direction of the photoelectrons will be discussed in section 4.2.3, where the initial conditions for the simulation are examined.

3.4 Secondary emission

The process of secondary emission follows a similar pattern as that of the photoemission from a photocathode and can again be divided into three steps. First, the primary electron deposits energy in the material freeing electrons from bound states. Secondly, these electrons need to diffuse through the material to the surface and lastly the secondary electrons will escape the surface if they have sufficient energy. The major differences to photoemission are that the incoming particle is now an electron and that it has $\sim$100 times more energy than the photon.[12] Therefore multiple electrons can be emitted.

The concept of the PMT multiplication system is based on the secondary emission, where each dynode multiplies the number of electrons according to the secondary emission yield δ of the material. A dynode usually consists of a substrate electrode material like nickel, stainless steel or copper-beryllium. A layer of secondary emission material is coated onto this substrate. The exact material used for the IceCube mDOM PMT is not known but typically materials such as alkali antimonide, beryllium oxide or magnesium oxide are used [30]. The result of a primary electron striking the dynode is shown in figure 3.4.1.

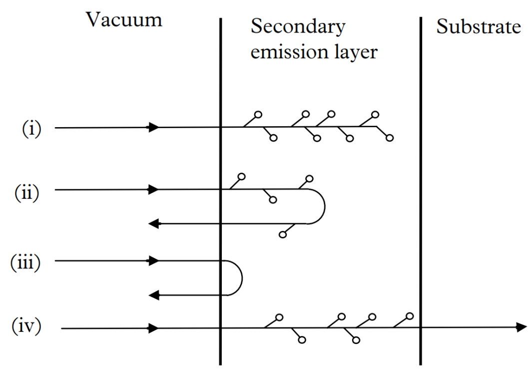

Figure 3.4.1: The four possible results from secondary emission. (i): Ordinary secondary emission where all the energy is deposited in the secondary emission layer. (ii) The primary electron produces some secondaries and is then inelastically scattered. (iii) The primary electron is elastically scattered from the surface. No secondaries are produced. (iv) The primary electron has enough energy to traverse the secondary emission layer into the substrate where no further secondaries can be produced. Image taken from [31].

There are four possible outcomes of secondary emission. In the default scenario the energy of the primary electron is completely deposited inside the secondary emission layer and some of the freed electrons will escape from the material into the vacuum. These electrons are sometimes referred to as "true" secondaries. There is also the possibility for inelastic scattering of the primary electron. When this happens fewer true secondaries will be emitted in addition with a single higher energy electron. Additionally, the primary electron can elastically scatter on the secondary emission surface and not produce any secondaries at all

[12] This depends on the voltage applied between the dynode stages

(on the first dynode this would result in a late pulse). If the primary electron has sufficient energy it will not deposit all its energy in the secondary emission layer of the dynode and traverse into the substrate. Here no more electrons will be freed from the material. Therefore the secondary emission yield decreases with very high electron energies.

It is important to note that the electrons won't hit the secondary emission layer perpendicular like shown in figure 3.4.1 but at an angle to the surface normal. This allows the primary electron to deposit more energy inside the secondary emission layer as the path through this layer is elongated. The secondary yield is further increased since the electrons will also be liberated closer to the surface and therefore have a higher chance of becoming true secondaries.

4 COMSOL Simulation

This chapter will give a brief introduction to COMSOL Multiphysics® in section 4.1, which will focus on the relevant topics for this thesis (see section 4.2). Some important aspects of the simulation and its limitations are described in section 4.3.

4.1 What is COMSOL and why would we use it?

COMSOL Multiphysics® (short COMSOL) is a proprietary software used to simulate processes in physics and engineering. It is a general purpose simulation software that uses numerical methods and covers a wide range of physics. These physical processes are governed by partial differential equations (PDEs) [13] which need to be solved in order to make calculations and predictions with them. Solving these equations analytically is usually impossible or at least not easily done.

COMSOL uses the **finite element method** (FEM) [32] to solve the PDEs of the physics involved in the simulation. This method divides the problem into smaller parts, the finite elements. On each of these elements the PDEs are then approximated numerically and the combined solution over all elements models the entire problem.

One of big selling points of COMSOL is that it is not limited to one "type" of physics. While it is perfectly capable of modeling single physics problems, it can also combine different physics fields into one model, like the surname Multiphysics implies. One could for example model the mechanical stress in some component that arises due to joule heating or like in the case of this thesis the movement of electrons inside of an electric field.

4.2 PMT Simulation in COMSOL

This section will introduce the simulation of the PMT in COMSOL. A complete description of the simulation would go beyond the scope of this thesis but the most important parts will be highlighted. For further information about COMSOL refer to [33].

For any simulation in COMSOL there are five parts without one of which the simulation will not compute. The **geometry** of the problem needs to be defined as well as the **materials** of all components in the model. In the case of the PMT simulation the materials do not change the physics simulated. Therefore, all objects in the simulation are defined as vacuum. Once geometry and materials are defined it is possible to select the **physics** one wants to simulate. This includes both the single physics and multiphysics interfaces. The level of discretization used in the FEM is set when building a **mesh**. COMSOL automatically builds a mesh depending on the included physics but it is also possible to create a mesh manually. Finally, the type of **study** to be performed needs to be selected. There are a plethora of studies available but for the PMT simulation only a *stationary* study for the computation of the electric field and a *time-dependent* study for the trajectories of the particles are needed.

[13] The Maxwell equations describing classical electromagnetism in combination with the Lorentz force are PDEs for example.

4.2.1 Geometry

The first step to creating a COMSOL simulation is to define a geometry. In the case of the PMT simulation, a real IceCube mDOM PMT was sent to the *ZEISS Quality Excellence Center* in Cologne [34] where a CT scan of the PMT was performed. With the geometry data of this scan a CAD file was generated and imported into COMSOL. The result of this endeavour is shown in figure 4.2.1. The accuracy of the CT scan is in the order of a few $10\,\mu\mathrm{m}$ so the confidence in the correctness of this geometry is high [35]. This will be further discussed in section 4.4.

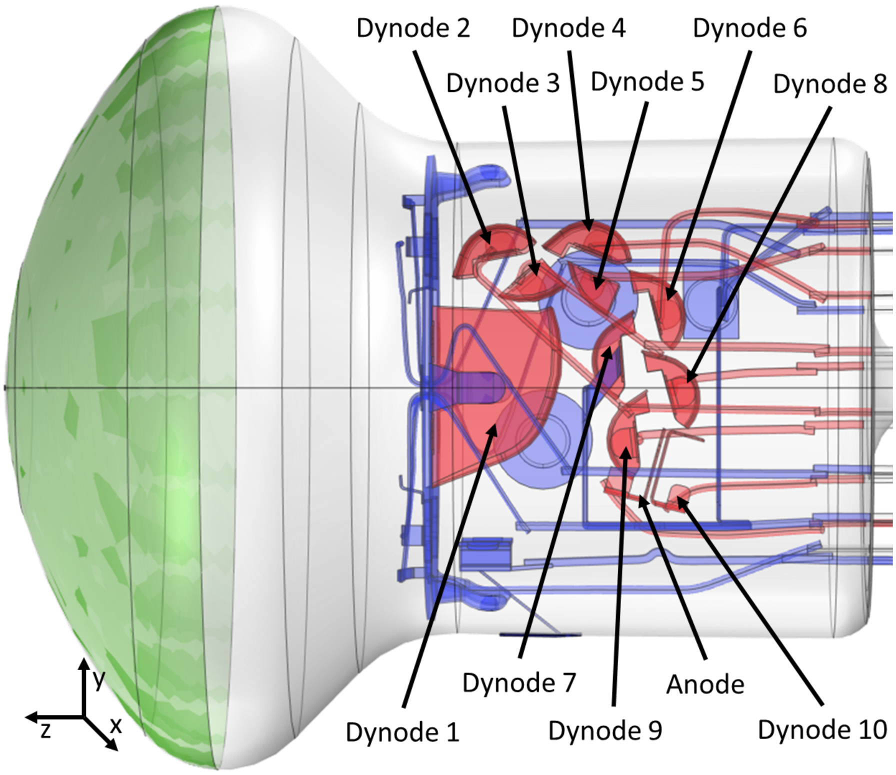

Figure 4.2.1: The geometry used in the simulation. The dynode system is colored red and the dynode numbers are given while other internal components are colored blue. The glass bulb is shown in white and the photocathode area is highlighted in green.

The dynode system in the geometry (highlighted in red) consists of the 10 stages mentioned in section 3.1 in combination with the anode and can be classified as *circular linear focused*. This results in the dynode system being more compact and the PMT smaller to fit into the mDOM. Apart from the dynode system there are some internal structures in the geometry, highlighted in blue. Some of these are not as important to the simulation as their only purpose is e.g. holding the photocathode material until it is evaporated onto the glass bulb or supplying the photocathode with power. One very important component however is the frontal plate (referred to in figure 3.1.1 as focusing electrodes). This plate is used to hold the dynode system inside the PMT in place. It has a rectangular hole in the middle underneath which the first dynode is located. The area of the photocathode is highlighted in green. Starting from this area the photoelectrons will make their way through the PMT.

Due to some physical limitations of the CT scanning process the geometry used in the simulation is missing some details. Some of these missing details can be seen by comparing figure 4.2.2a and figure 4.2.2b.

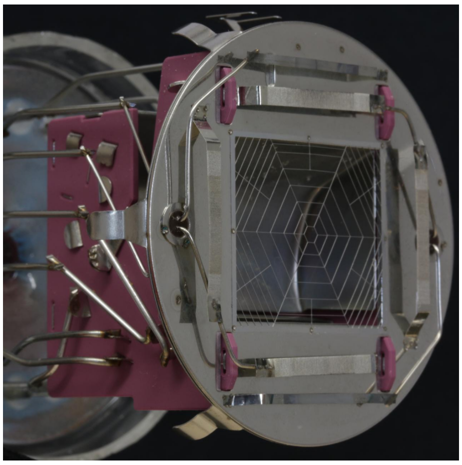

(a) View of a real PMT with the glass bulb removed. Image courtesy of the IceCube collaboration.

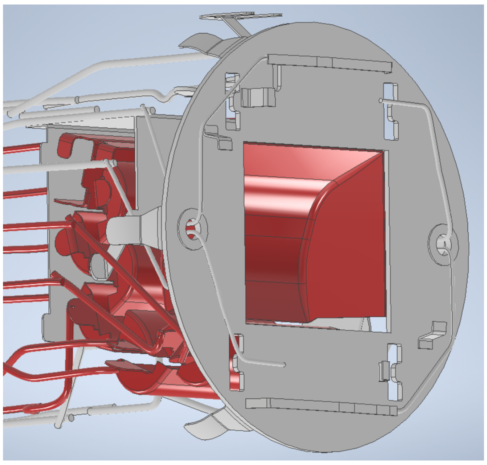

(b) View of the CAD model in Autodesk Inventor [36]. The dynodes are highlighted in red. The glass bulb is not shown.

Figure 4.2.2: Comparison between the internal components of a real PMT in figure 4.2.2a and the CAD file in figure 4.2.2b. The main difference are missing structures on the frontal plate as well as missing ceramic panels to the side of the dynode system.

The first picture is taken from a real PMT where the glass bulb has been removed, while the latter shows the CAD file from a similar angle. Two main differences can be identified.

1. The CAD file is missing some structures on the frontal plate. The intended use of some of these structures is unclear. Namely the rectangular shaped electrodes that surround the opening towards the first dynode. There is another electrode in the shape of a spider web in this opening. It is thought that this should enhance the timing characteristics of the PMT. When looking at the PMT in real life it becomes clear that all these components are at the same potential as the first dynode. Due to the thinness of these structures, they were not clearly visible in the CT scan and therefore omitted in the CAD reconstruction. Additional efforts will need to be made to include them.

2. The dynode system in the CAD file is open to the sides while that of the real PMT is closed of by two ceramic plates. These have the purpose of preventing secondary electrons from spreading outside of the multiplication system as well as holding the dynodes in place.

There is another discrepancy between the CAD file and the real PMT in the shape of the anode. As can be seen in figure 4.2.1 the anode is located in front of the tenth dynode. This is done to reduce the space charge effect from millions of electrons [29]. To still have the last dynode contribute to the multiplication process the anode has a structure like shown in figure 4.2.3.

The main anode surface has hexagonal holes in it to let electrons pass through to the last dynode and then be collected. The close proximity between the anode and last dynode will result in a large electric field gradient reducing the space charge effect.[14]

In the CAD file the anode is made without these holes. But as the space charge effect will not be modeled in the simulation [15] this only changes the simulation results in regard to the final arrival time of the electrons. Since the position of the anode is closer to the tenth dynode this effect should be small.

[14] Due to the large number of electrons the effective electric field strength is lowered.

[15] In section 4.3 more details about this are given.

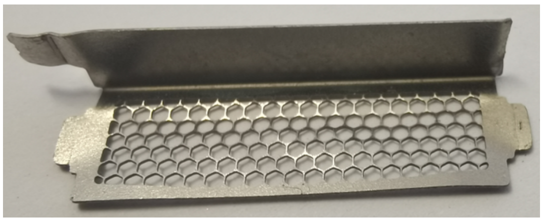

Figure 4.2.3: Shape of the anode of the IceCube mDOM PMT taken from a disassembled PMT.

4.2.2 Physics

The physics included in the simulation consist of two interfaces. Namely the *electrostatics (es)* and the *charged particle tracing (cpt)* interface.

The use of the *es* interface is rather straight forward. With the *electric potential* boundary condition one can apply any electric potential to any boundary. With this, the boundaries of the components shown in figure 4.2.1 are applied the corresponding voltage described in section 3.1. The supply voltage used in the simulation is $1200\,\mathrm{V}$. The electric field inside the PMT is then calculated using

$$\mathbf{E} = -\nabla V \tag{4.2.1}$$

with V being the potential applied. When initializing the interface COMSOL automatically applies charge conservation across the whole geometry.

The movement of the electrons inside the PMT is defined in the *cpt* interface. Here some general settings like the use of relativistic correction can be selected as well as the particle type which is set to the electron. These are initially generated at the photocathode using an *inlet* boundary condition. In this node the initial conditions of the photoelectrons can be applied and selected. Another boundary condition is the *wall* node. This stops particles when they hit the applied boundary. The *wall* node has a sub node called *secondary emission* which can be used to implement the gain of the PMT. In this sub node the initial conditions for the secondary electrons are assigned. The coupling between the *es* and *cpt* interfaces is done with an *electric force* domain property in the *cpt* interface. Here the electric field calculated with the *es* interface is taken as an input for the particle tracing studies. The movement of the particles is modeled by

$$\frac{d(m \cdot \mathbf{v})}{dt} = \mathbf{F} \quad \text{with} \quad m = \frac{m_r}{\sqrt{1 - \frac{v^2}{c}}}. \tag{4.2.2}$$

Where m_r denotes the rest mass of the particle, v the velocity, c the speed of light in vacuum and F the forces acting on the particle. In the *electric force* node this force is given by

$$\mathbf{F} = eZ\mathbf{E}, \tag{4.2.3}$$

with e the elementary charge, $Z = 1$ the charge of the electron and $\mathbf{E}$ the electric field. This equation of motion is then solved to obtain the trajectories of the particles.

4.2.3 Initial conditions

The initial conditions of the simulation play a central role and are one of the sources of systematical bias as they directly influence the behaviour of the electrons. It has been shown in previous works that the wavelength of the incoming photon has an effect on the PMT properties [22]. Therefore, accurate initial conditions for the photoelectrons have to be defined.

Position

The initial position of the photoelectron is mostly dependent on the study one wants to perform. In previous studies the photocathode is illuminated with different light patterns [22, 37]. This can be split into two groups and is shown in figure 4.2.4.

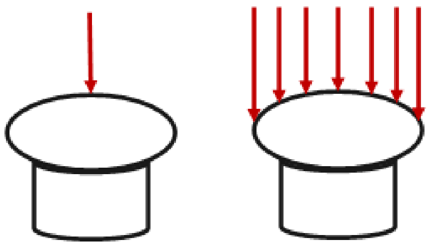

Figure 4.2.4: Scematic drawing of the two different illumination patterns for PMT characterization. Left shows the single point illumination and right the illumination of the full photocathode.

First, there is the illumination of the whole photocathode and secondly, there is the illumination of only a small portion of the photocathode. The first method is usually used to characterize PMTs in bulk, i.e. when the mDOM or other modules are calibrated. The latter method gives a deeper understanding about the characteristics of PMTs in general but is more time consuming and therefore not used for bulk characterizations. COMSOL allows for the initial position to be selected from both a boundary and a point. This way both of these illumination patterns can be simulated.

Energy

The selection of the initial energy can be seperated into two parts. First, there is the energy distribution of electrons when they exit the photocathode. Then there is also the dependence of this distribution on the wavelength of the incoming photon.

The model of the initial energy for photoelectrons is described in section 3.3. The photon needs to have a minimum energy E_{ph} of

$$E_{\text{ph}} \geq E_g + E_a = \Phi, \tag{4.2.4}$$

where E_g denotes the energy of the band gap and E_a the electron affinity of the material to liberate an electron from the material. These two values are combined into the work function Φ of the material. For a realistic modeling, the work function would need to be corrected due to impurities, surface roughness or external electric fields. If the photon energy is greater than the work function, an electron can be emitted from the material with the energy

$$E_e = E_{\text{ph}} - \Phi \geq 0. \tag{4.2.5}$$

Therefore, the wavelength range a photocathode is sensitive to depends on the work function of the material.

As stated in section 3.3, the photon will lose energy on its way towards the surface. Equation (4.2.5), therefore, only provides the upper limit for the electron energy. Actual measurements of the energy distribution of photoelectrons are scarce as most of the time only the spectral response [16] of photocathodes is of interest. In the case of the IceCube mDOM PMT, a bialkali photocathode is used for which specific measurements are even harder to find. For the photon energies of interest (between $300\,\mathrm{nm}$ [17] and $650\,\mathrm{nm}$ [18] [30]) the energy distribution follows a Gaussian like behaviour with a single peak. The position of the peak rises monotonically with the photon energy [38]. Additionally the width of the distribution increases linearly with the photon energy [39]. The data of the energy distribution of a K_2CsSb photocathode is extracted from [38] and presented in figure 4.2.5.

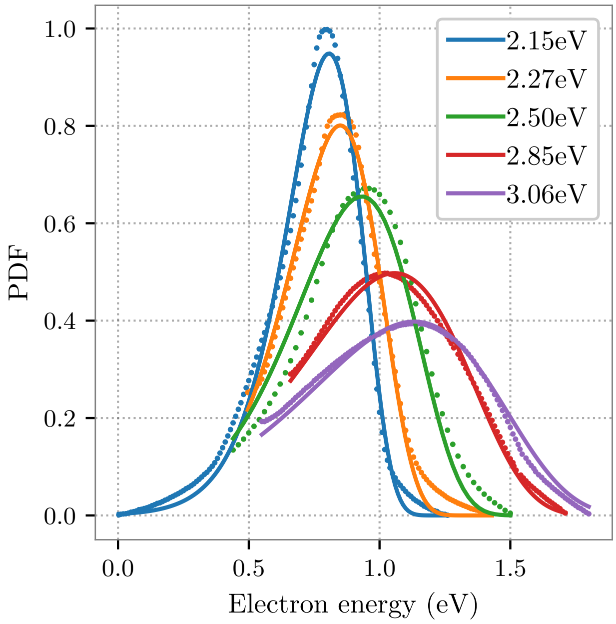

Figure 4.2.5: The energy distributions used for the PMT simulation from a K_2CsSb photocathode. The data taken from [38] is fitted using equation (4.2.6). No uncertainties are assumed as the goal is just to get the general shape of the distributions and not to replicate them.

The measured curves follow the above described shape. It is important to note that the intensity goes to 0 for photoelectron energies approaching $0\,\mathrm{eV}$. This is likely due to the opposing field method used in this measurement which is known to be inaccurate for low electron energies [40].

To implement these curves into COMSOL a fit of an asymmetric generalized normal distribution of the form

$$F(x,\mu,\sigma,\mathrm{A},\gamma) = \frac{\mathrm{A}}{\sqrt{2\pi}} \begin{cases} \frac{1}{\sigma}\exp\{-\frac{(x-\mu)^2}{2\sigma^2}\} & \text{,if } \gamma = 0 \\ \frac{1}{\sigma-\gamma(x-\mu)}\exp\{-\frac{1}{2\gamma^2}\ln\left[1-\gamma\frac{x-\mu}{\sigma^2}\right]^2\} & \text{,if } \gamma \neq 0 \end{cases} \tag{4.2.6}$$

$$\mu(\lambda) = a\cdot\lambda + b$$

$$\sigma(\lambda) = c\cdot\lambda + d$$

[16]The spectral response of a PMT describes how likely it is to generate a pulse depending on the incoming photon energy.

[17]This is limited by the transitivity of the glass.

[18]This is limited by the work function of the material.

Table 4.2.1: Obtained fit values for the distribution of the initial photoelectron energy.

Parameter	Value
a [$\mathrm{eV\,nm^{-1}}$]	(0.29 ± 0.01)
b [eV]	(0.14 ± 0.01)
c [$\mathrm{eV\,nm^{-1}}$]	(0.26 ± 0.01)
d [eV]	(-0.41 ± 0.01)
γ	(0.27 ± 0.01)

to the measured data is performed using the python package *lmfit* [41]. Here μ is the mean, σ the width and γ the shape of the distribution. a, b, c and d are the parameters for the linear dependence between wavelength λ and μ or σ respectively. A is a nuisance parameter to scale the functions. The resulting parameters of the fit are listed in table 4.2.1 and the fit itself can be seen in figure 4.2.5.

The obtained function is then imported into COMSOL using the method described in [42]. It again needs to be highlighted that the true material of the IceCube mDOM PMT is not known. Therefore it is not necessary for the fit to represent every detail of the measured data, but only to accurately follow the shape described in the literature.

Direction

The initial direction of photoelectrons is described by a Lambertian distribution [31]. This states that the intensity of radiation emitted from a surface is proportional to

$$I \propto I_0 \cdot \cos\theta, \tag{4.2.7}$$

where I_0 is the maximum intensity and θ is the angle to the surface normal. It is also known as Lambert's cosine law or the cosine emission law and directly supported in COMSOL.

Secondary particles

The initial conditions of secondary particles are not implemented in the simulation properly. Their starting position will be the hit position of the incoming electron but their initial energy is set to $0\,\mathrm{eV}$. This way the secondary electrons will only move according to the electric field and an initial direction is not needed. Additionally, every primary electron will produce exactly one secondary electron.

The proper implementation of the initial conditions for the secondary particles is not trivially done in COMSOL. As described in section 3.4, there are three different types of secondary particles. The true secondaries, the inelastically scattered electrons and the eleastically scattered electrons. The distribution of the initial energy would need to account for all three of them. Additionally, the number of secondary particles depends on the energy and angle of incident of the primary electron. One also needs to consider energy conservation. The combined energy of all secondaries should not exceed the energy of the primary electron. All these contributions lead to a complicated way of sampling the initial conditions of the secondary electrons.

4.2.4 Studies

The PMT simulation is performed in two separate steps. First, the electric field is calculated using a *stationary* study. The solution of this is then passed to the *time dependent* study for the computation of the electron trajectories. The details of these studies will not be discussed as they are also only slightly modified from the initial settings done by COMSOL.

Generally, there are two types of solving algorithms. Both of them aim to solve the linear matrix equation $Ax = b$ through different means. In FEM problems A is referred to as the stiffness matrix and b the force vector while x is the set of unknowns one wants to obtain. The equation can be solved either directly or iteratively. The *stationary* study uses a direct solving algorithm called MUMPS [43] where the solution is obtained by factoring and then inverting the matrix A.

The second type of solvers are the iterative solvers, where an initial guess x_0 to the solution of the linear matrix equation is computed. Then $r_0 = b - Ax_0$ is calculated and minimized in multiple steps according to the scheme of the specific solver. The iterative solver GMRES [44] is used in the *time dependent* study for the electron trajectories.

The trajectories of the electrons are described by equation (4.2.2). COMSOL solves this equation also iteratively. To do this, the position and velocity of the particles as well as the forces acting on them are used to calculate the movement of the particles in a discrete time step. This time step is determined using the Generalized-alpha method [45]. After a series of time steps [19] the full trajectories of the particles are calculated. The size of the time steps used in this method is selected by the algorithm based on an estimation of the errors in relation to the tolerances set by the user or COMSOL [46]. It is also possible to manually set the time steps although it is not recommended [47].

4.3 Limitations of COMSOL

During the setup of the simulation, several difficulties were encountered, some of which are not trivially solvable. This section aims to provide an overview of the features that are still missing in the simulation due to either hardware or software limitations.

4.3.1 Limitations by hardware

The limitations by hardware focus mostly on the system resources available when trying to run a simulation or extract data from it. The most important system resource for COMSOL is the available memory, or RAM. This memory has the fastest connection to the central processing unit (CPU). Should its resources be exhausted, additional space will be used in what is called virtual RAM. This is essentially disk storage which is considerably slower than RAM. Therefore, solving a model that uses more memory than RAM installed will run significantly slower [48].

The exact amount of memory needed per particle always depends on the simulation, since other parameters such as the mesh will also have an influence. If a finer mesh is used in the simulation more memory will be needed for the calculations. There is always a ground level of memory usage when running a *time dependent* study. This dominates the memory requirement for lower numbers of particles as can be seen in figure 4.3.1.

Here the required memory is plotted against the total amount of particles in the PMT simulation for the *time dependent* study. A linear fit is performed and the slope is determined to be $(4.78 \pm 0.07)\,\mathrm{kB/particle}$ with a y-intercept of $(10.62 \pm 0.11)\,\mathrm{GB}$.[20]

[19] For the PMT simulation this is usually around $35\,000$ time steps.

[20] For this data COMSOL version 6.1.0.357 is used. In a previous version the memory usage is less optimized.

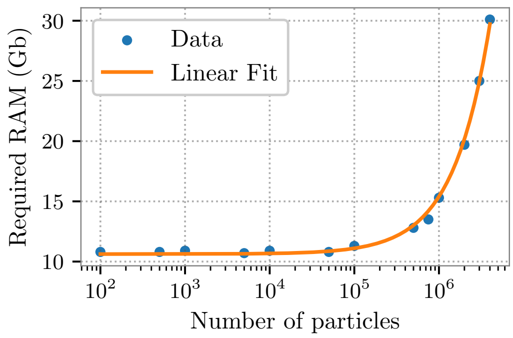

Figure 4.3.1: Required memory for the *time dependent* study in the PMT simulation against the total number of particles in the simulation. A linear fit is performed to the data. Note that the x-axis is in logarithmic scale.

With this fit it is possible to estimate the memory requirements for the full PMT simulation.[21] The nominal gain of the IceCube mDOM PMT is $5 \cdot 10^6$. This is the amount or particles that arrive at the anode. To calculate the total number of particles in the simulation the previous amplification stages need to be added to that number as well.

The total number of particles can be estimated to about 6.3×10^6 by assuming a multiplication of $\sqrt[10]{5 \cdot 10^6} = 4.68$ electrons for each dynode. As mentioned in section 4.2.1, the last dynode does not contribute to the multiplication process in the simulation. Removing the last multiplication step lowers the total number of particles to about 1.4×10^6. This would result in a RAM requirement of about 17 GB for a single photoelectron pulse to solve the study.

After the simulation is completed the data will be stored on the disk. These files can be rather large (up to several 100 GB) as they store the full trajectory of every particle along with other information. As mentioned in section 4.2.4, there are several time steps required to reconstruct the trajectory. When extracting data from a simulation, this needs to be kept in mind so as to not overwhelm the system resources. Usually, only the last time step is exported to data. This contains information about the final status of all particles in the simulations such as their energy, position or arrival time. This data will be used for the analysis of the PMT properties. It is also possible to export the whole trajectory of particles, which is only done for small numbers of particles (up to 1000 in total).

The runtime of the simulation also increases with the number of particles in the simulation. Other parameters such as the mesh size or a constraint on the time steps in the solver also impact this. The exact amount of time necessary to compute a study always depend on the machine the study is run on and universal numbers can not be given. Generally, the runtime is said to scale linearly with the number of particles as long as sufficient RAM is available.

4.3.2 Limitations by software

The limitations by software focus more on the involved physics or used study. The first thing to mention is that this simulation only performs electron propagation. This is due to the absence of a suitable interface in COMSOL that combines the propagation of photons and electrons as well as an interface that converts photons to electrons using the method described

[21] The data is acquired by starting a simulation with the total number of particles starting from the photocathode and multiplication disabled. The simulation is also stopped after a few time steps as the computation time rises rapidly with the number of particles. Thus this estimation does not include any unforeseen contributions during the solving of the study.

in section 3.3. This means that the simulation starts at the end of the photoemission process with electrons which have the initial conditions described in section 4.2.3.

Another limitation is connected to the evaluation of simulation results. As described in section 4.3.1, only the last time step is exported and used for the analysis. This time step contains information about the final status of the particle like the final position, energy, arrival time, time of flight and trajectory length. It is however not possible to export the initial conditions for all particles easily. For primary particles this can be done, since the time of their creation is exactly known. The information about the initial position is missing for secondary particles. One possible work around to obtain this information would be to export all time steps and then select the first occurring value for the secondary particles as their initial position. This leads, however, back to the limitations by the hardware. Another work around is to segment the photocathode into smaller parts and run multiple simulations in parallel. This way, some information about the position can be preserved.

The multiplication in the simulation is limited as there are too many dependencies between the properties of the primary electron (energy and incident angle) and the number and properties of the secondary electrons. To model each of these on their own would be a possibility but the combination of them would pose further challenges [22]

Finally, COMSOL does not provide uncertainties to any of the values. Uncertainties in COMSOL arise from the different parts of the simulation. The discretization of the geometry into the mesh introduces errors as well as the discretization of the time. Additionally, the solver for the respective study has inhering numerical uncertainties that are not disclosed. No quantification for the uncertainty will be done in this work. Therefore, uncertainties in the following chapters are rarely present and when given arise from fits of distributions to data or calculations of mean values or standard deviations [23]

4.4 Old vs. new geometry

During the time of writing this thesis, two geometries of the PMT are used. The first geometry was created for studies on the influence of external electric fields on the internal electric field of the PMT in [49]. The second geometry is described in section 4.2.1 and was obtained by CT scanning a PMT.

A previous study was performed using the first geometry with the exception that only the area of photocathode and first dynode were imported into COMSOL [50] [24] In the beginning of this thesis the previously set up simulation was rebuild with the implementation of the full geometry. After initial trials it became clear that the geometry was not suitable for the simulation of the whole PMT as electrons would not propagate further than the third dynode.

This effect is demonstrated in figure 4.4.1a and figure 4.4.1b where the dynode system of the old CAD file is used. The other components of the PMT were built manually. Additionally, the electrons at the photocathode start with an energy of $1\,\mathrm{eV}$ normal to the surface and the multiplication factor on each dynode is set to 1. The simulation is shown in 2D in order to enhance the visibility of the effect.

[22] For example tracking the secondary particles back to their origin is not easily done. One would need to simulate the photoelectrons one by one to circumvent this problem. Additionally, the space charge effect of the electrons would need to be included further increasing the memory requirements and computational time.

[23] There is a package for COMSOL called the *Uncertainty Quantification Module*. However, this is used to determine the impact of uncertainties in initial conditions and not extract those of the simulation.

[24] This was due to a licensing issue and has since been resolved.

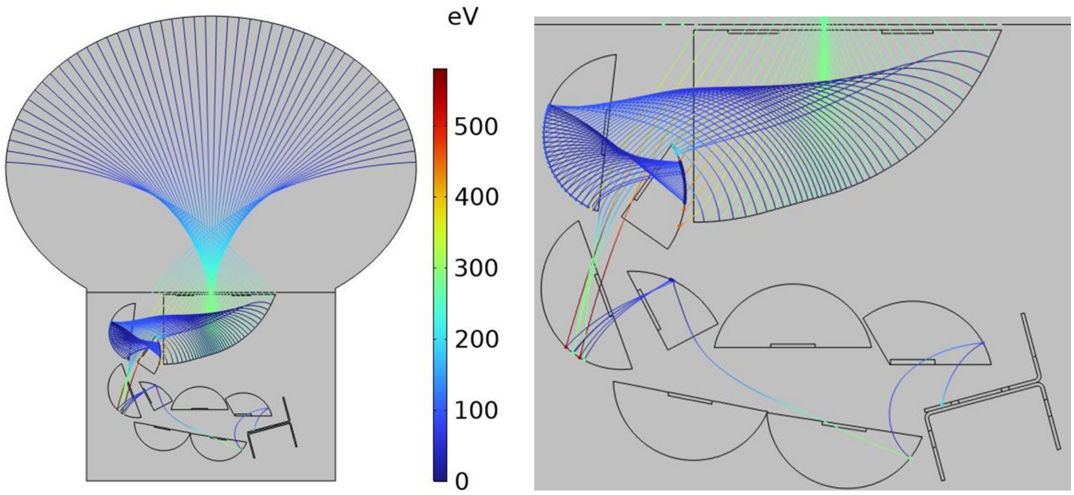

(a) Full picture.

(b) Magnification of dynode system.

Figure 4.4.1: Simulation of the electron trajectories in the old dynode system in figure 4.4.1a. The dynode system is taken from the CAD file while the rest is build manually to show the effects described in the text. The colorbar indicates the particle energy. Figure 4.4.1b shows an enlarged view of the dynode system.

The reason for not propagating further is that these particles are deleted by COMSOL in the simulation. This happens when a particle remains at some position for a number of time steps and is done to decrease the computation time and memory usage. The initial guess for the occurrence of this effect is that the simulation resolution of the electric field is too low and the field from second to third dynode pushes the electrons towards the surface of the third dynode more than the field from third to fourth attracts the electrons. This low accuracy was compensated by using a much finer mesh but yielded the same result. Additionally, the initial energy of the secondary particles is increased with no effect.

When comparing the CAD file of the first geometry with parts from a disassembled PMT the shape of the dynode does not match since in the file they are modeled as simple half circles but in reality extend further in the direction of the previous dynode. Additionally, it is found that the successfully propagation of electrons in COMSOL is sensitive to a precise alignment of the electrodes. This is seen by moving the position of the dynodes in the order of $1\ \mathrm{mm}$ with vastly differing results. By manually changing the position of the second, third, fourth and fifth dynode it is possible to obtain propagation of electrons from the third to the fourth dynode.

All this lead to the conclusion that the shape and position of the dynodes in the multiplication system are not accurate enough to calculate the electron trajectory properly. To obtain a better geometry, a PMT was sent for CT scanning with the resulting geometry shown in section 4.2.1. A direct comparison of the dynode system of both geometries is shown in figure 4.4.2.

It is evident that the shape of the dynodes differs significantly between the geometries. The first dynode of the current geometry extends further into the multiplication system than in the old geometry where it is shallower. Dynodes two through nine also extend into the direction of the previous dynodes. These changes result in the propagation of the electrons through the whole PMT as will be seen in the following chapters.

When comparing the two geometries in figure 4.4.2 it becomes clear that the old geometry is more detailed when it comes to the structures on the frontal plate. The electrodes are visible

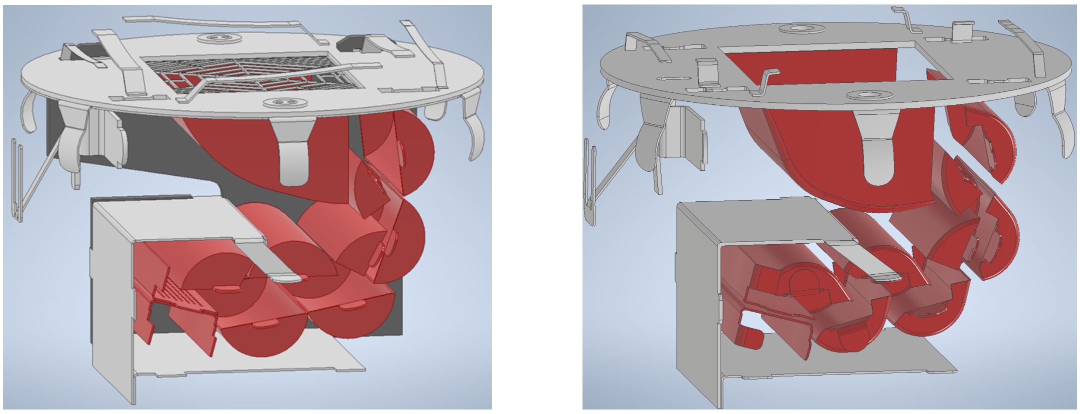

(a) Old geometry.

(b) Current geometry.

Figure 4.4.2: The two geometries used for the PMT simulation. Figure 4.4.2a shows the previously used geometry created by [49] while the current geometry is visible in figure 4.4.2b. It was obtained by CT scanning a real PMT. The dynode system is highlighted red and some details are removed to better compare the dynode system. The glass bulb is not shown.

and the spiderweb in front of the first dynode is also present. In the previous COMSOL study the influence of the frontal plate and the spiderweb on the performance of the PMT was investigated [50]. It was shown that the influence of the spiderweb in front of the first dynode in the old geometry was very little when looking at the collection efficiency of the first dynode ($0.01\,\%$ change), the transit time to the first dynode ($0.15\,\mathrm{ns}$ change) and the transit time spread ($0.04\,\mathrm{ns}$ change). Additionally, the thickness of the spiderweb in the old geometry is $0.2\,\mathrm{mm}$ while in reality the wires are much thinner, in the order of $10\,\mathrm{\mu m}$. The impact of the other structures on the frontal plate were not estimated but are not expected to be relevant.

5 Quality Control

This chapter addresses the quality control performed to investigate the validity of the results of the simulation. First, the parameters that are controlled will be explained in section 5.1 and the procedure to investigate them in section 5.2, followed by the impact of different meshes and solver settings in section 5.3 and section 5.4 respectively. Lastly, section 5.5 elaborates on the reliability of the final simulation configuration with these control parameters.

5.1 Control parameters

The objective of the quality control is to assess the simulations ability to accurately replicate the trajectories of the electrons inside the PMT. Several parameters can be studies to control the accuracy of the simulation. In this thesis, however, the focus is mainly on the **energy** and secondly the **position** of the particles.

The first parameter to be observed is the energy of the particle along its trajectory. When an electron travels inside of a static electric field, its energy can be exactly determined by adding the initial energy of the particle to the potential at the current position. Thus it is possible to study how well the energy is conserved in the simulation and give an estimation of the impact on timing as well as gain. Energy conservation is a beneficial trait as it allows for the determination and comparison against the true value. It is important to keep in mind that the electric field inside the PMT is not known for every point. The electric potential is extracted from COMSOL. A comparison therefore only shows how well COMSOL conserves the energy of the particle with respect to its own electric field calculation.

Additionally, one can consider the final position of the particles. As discussed in section 4.4, slight modifications to the geometry of the PMT can determine whether the propagation of secondary electrons towards the next dynode is successful. The position of the particles should be impacted by the solver as little as possible. This value is not easily quantified as the true value of the particles final position is not known. The investigation of the simulation accuracy will, therefore, focus on the energy conservation.

As PMT properties such as the timing and collection efficiency are subject of this thesis, the impact of the simulation accuracy on them will also be investigated through the two parameters above.

5.2 Procedure

In order to show the change of the above mentioned parameters depending on the used mesh or simulation settings, the simulation is first simplified by changing the initial conditions for the photoelectrons. These were released from a central point on the photocathode with an energy of $1\,\mathrm{eV}$ in a direction normal to the surface. The initial conditions for the secondary electrons remained unchanged. An example of the simulation with such initial conditions is presented in figure 5.2.1.

These changes to the initial condition result in the released particles following strictly the electric field lines in the PMT, meaning that the results between different simulation settings

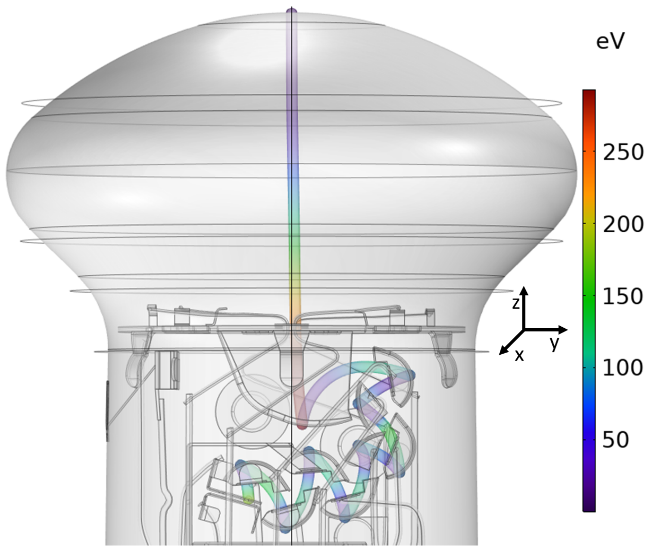

Figure 5.2.1: Simulation result for the simplified initial conditions used for the quality control. The colorbar indicates the particle energy along the trajectroy in eV. The width of the partile trajectory is increased to improve the visibility.

are comparable. This also means that simulating more than one particle does not yield additional information as all these particles move on the exact same trajectory.[25]

After the simulation is finished, the particle data is extracted. This can be done in COMSOL, however, is limited in the amount of information accessible as described in section 4.3. It is also possible to extract the particle data via the python package *MPh* [51]. This method allows for extraction of the full particle information but it is limited to small numbers of particles due to memory constraints. As the number of particles simulated in this section is small, however, this constraint is negligibly.

With the full particle trajectory information available, the position and energy of every particle for each time step taken by the solver can be accessed. To calculate the energy conservation, the particles position is imported into COMSOL and the electric field at these positions is calculated and then exported. By comparing the electric potential with the observed energy of the particles at a given position, the energy conservation is investigated. A possible result of this is shown in figure 5.2.2. Here, the data of an electron traveling from the photocathode to the first dynode is used. The x-axis corresponds to the absolute time in the simulation.

The expected energy E_f (denotes as *Field*) describes the energy that the particle should have according to the electric potential at its position and initial energy, while E_p (denoted as *Particle*) is the energy that the particle has according to the simulation. Both of these energies follow the same shape and the absolute difference $E_p - E_f$ is used to quantify the energy conservation. The latter is shown on the second graph of figure 5.2.2 and it is small when compared with the final energy of the particle of almost $300\,\mathrm{eV}$.[26]

One noteworthy feature of figure 5.2.2 is the slight bump in the energy at the end of the propagation close to the dynode. This is present in most dynodes and caused by the attracting electric field of the other dynodes.[27] This accelerates the particles over the potential of the targeted dynode. Consequently, the particle is decelerated for the last part of its trajectory.

[25] To be sure ten electrons are released for each study.
[26] Note that for the other dynodes this will be about three times smaller.
[27] Usually only the next or next but one dynode is responsible for this.

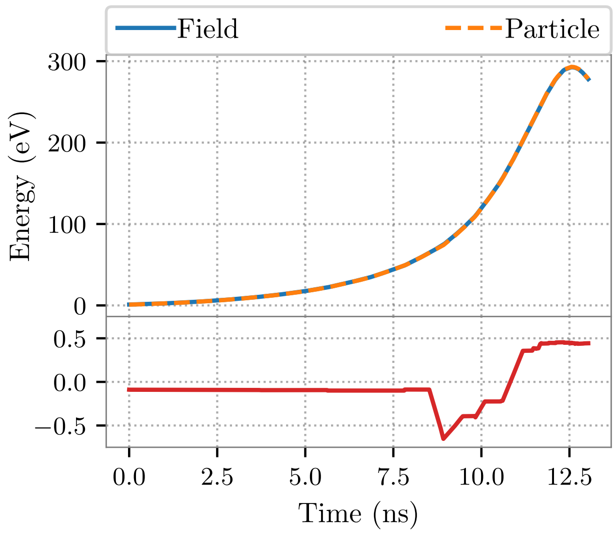

Figure 5.2.2: The expected energy of the particle due to the field and the actual energy of the particle against the time of flight in the PMT. The second line below shows the difference between the two energies. Data taken from the trajectory between the photocathode and first dynode.

This is also believed to be the cause for the non straight trajectory of the particle between the photocathode and first dynode (see figure 5.2.1) where the particle moves slightly in positive y-direction.

With the energy of the particle further statements can be made about the accuracy of the simulation. First, there is the potential impact on the gain and secondly, the impact on the arrival time of the particles.

As shown in section 3.2.1, the gain of the PMT depends on the supply voltage. This is due to the dependence of the secondary yield δ on the energy of the particles. This relation is usually described by a power law

$$\delta = \alpha \cdot E^{\beta}, \tag{5.2.1}$$

where α is a material dependent parameter and β ranges between 0.65 and 0.75 [29]. E is the energy of the particle from the energy conservation of which the impact on the gain can be calculated using

$$G = \frac{E_p - E_f}{E_f}. \tag{5.2.2}$$

Here a value of $\beta = 1$ is assumed so that δ is equal to the energy [28] to simplify the equation and give a more conservative value. A $G \leq 1$ would result in a smaller gain and $G \geq 1$ in a higher gain than expected. With this metric only the final status of the particle is important as this is when the multiplication would occur. In the exemplary case shown above a value of $G = 1.0016$ is obtained meaning the gain would be slightly above the expected value due to the particle having more energy than it should have.

Similarly, the arrival time of the particle can be probed. Through the kinetic energy of the particle the velocity is calculated. When comparing the trajectory length with the velocity,

[28] Note that α is factored out by the fraction.

the time of flight of the particle can be calculated with

$$t(E) = \sqrt{\frac{\Delta s^2 m_e}{2E_{\text{kin}}}}. \tag{5.2.3}$$

Here, Δs is the distance traveled by the electron, m_e its mass, and E_{kin} the kinetic energy. Lastly, the difference in the time of flight due to the difference in energy from the energy conservation is calculated with

$$\Delta t \equiv t(E_p) - t(2E_p - E_f). \tag{5.2.4}$$

This is done for every time step in the simulation. With the data of figure 5.2.2 this would correspond to the graph presented in figure 5.2.3.

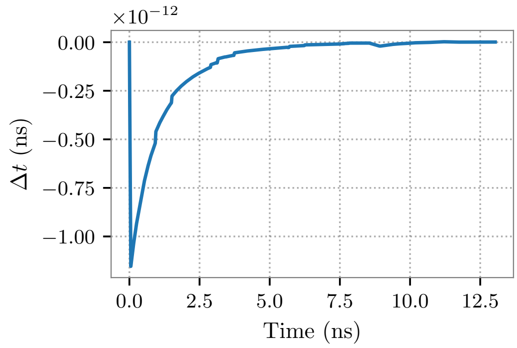

Figure 5.2.3: Difference in time of flight of the electron resulting from the energy conservation calculated using equation (5.2.4).

The time difference is largest at the beginning of the trajectory as the absolute difference between E_p and E_f is large compared to the absolute energy, while at the end of the trajectory the absolute difference (less than $1\,\text{eV}$) is small compared to the particles energy (up to $300\,\text{eV}$). The impact of the simulation settings on the time is seen by calculating the sum of the timing difference over all time steps. For the given example this results in a $-6.8 \times 10^{-2}\,\text{ns}$ shorter time of flight at the first dynode. It needs to be kept in mind that the rest of the multiplication system also contributes to the timing accuracy as will be shown in the following sections.

5.3 Impact of different mesh size

When running simulations with COMSOL the geometry is discretized by the mesh. This can be done automatically by COMSOL according to the physics involved in the simulation. There are predefined element sizes that range from *Extremely Coarse* to *Extremely Fine*. For the PMT simulation the mesh can only be built by COMSOL with element sizes *Finer*, *Extra Fine* and *Extremely Fine* as some structures of the PMT are too small for any coarser mesh. Additionally, a user defined mesh is created which uses different sizes for the various components of the PMT. The dynode system is set to the *Extremely Fine* setting while the glass bulb is set to *Extra Fine*. This has the advantage of higher precision for the important parts of the electron propagation while keeping the memory footprint and computation time for the studies considerably lower than for the *Extremely Fine* mesh. The corresponding mean element size as well as the time necessary to run the two studies with the respective

Table 5.3.1: Mean element sizes and computational time of the *stationary* and *time dependent* study for the different meshes sorted with ascending runtime.

Mesh	Element size (mm)	*stationary* (s)	*time dependent* (min)
Finer	1.18	15	4
Extra Fine	0.55	110	17
Custom	0.28	120	22
Extremely Fine	0.19	1320	110

meshes is listed in table 5.3.1. The runtime should not be used for any other comparison, though, as it is highly dependent on the machine used.[29]

The impact of these meshes on the simulation results will be investigated in the following sections with the exception of the final particle position as the results are not comparable due to the different element sizes of the meshes. The final particle position is consistent within a few $0.1\,\mathrm{mm}$ across the meshes, though.

5.3.1 Electric field

The first comparison of these meshes is done with the resulting electric field. To do this, point clouds are generated and the electric field at each of the points is exported from COMSOL. The points between the meshes is identical and the exported potential is then compared. Since there is no true value known, the meshes are compared against the *Extremely Fine* mesh as this theoretically has the highest accuracy. Deviations from a real PMT can not be excluded though. The result of this comparison is shown in figure 5.3.1.

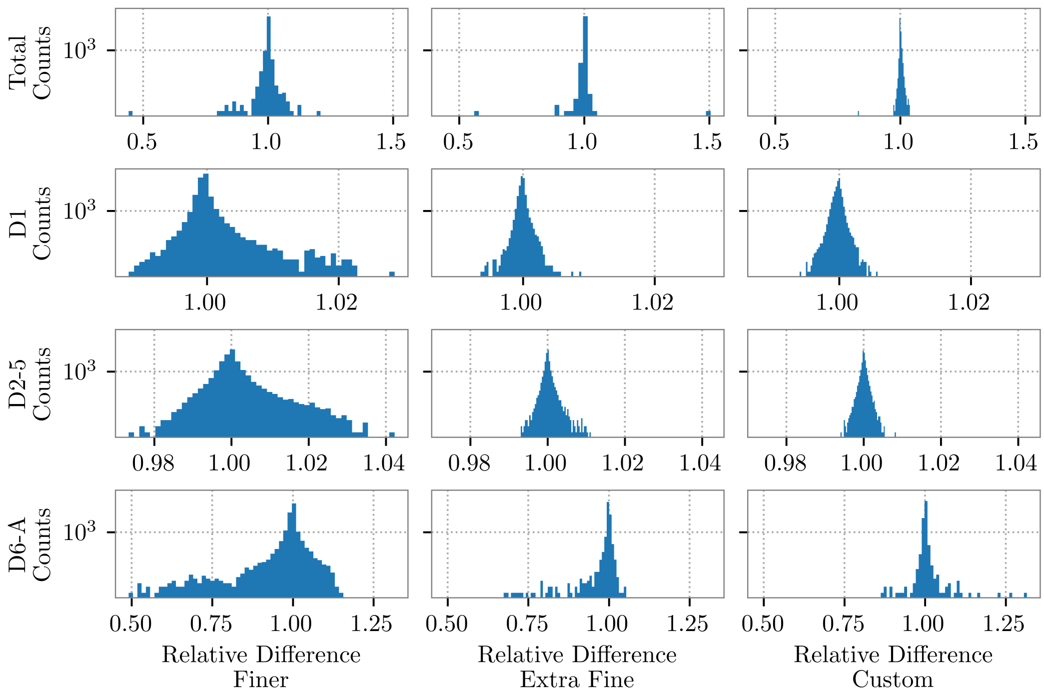

Figure 5.3.1: Comparison of the meshes in the simulation. The *Extremely Fine* mesh is used as a reference to calculate the differences to the other meshes. Plotted is a histogram of the relative deviations in the returned electric potential from COMSOL for four different regions inside the PMT. The rows of the plot correspond to the same region while the columns represent the same mesh.

[29]Here ten cores of an Intel Xeon W-2275 CPU equipped with 64 GB of RAM are used.

Four different regions of interest (corresponding to the rows in the figure) are studied. The histograms show the relative deviations of the mesh (corresponding to the columns in the figure) to the reference mesh. The first region (denoted "Total") contains the whole PMT but has a lower point density than the rest. The second region includes the first dynode as well as the area above it (denote "D1"). The last two regions are divided to the remaining dynodes with one holding dynodes two to five (denoted D2-5) and the other consisting of dynodes six to the anode (denoted D6-A). The *Extremely Fine* mesh is not shown as it serves as the reference value for the comparison.

The *Finer* mesh has the largest deviations from the reference mesh in all regions. The *Extra Fine* mesh adheres closer to the reference in general and improves compared to the *Finer* mesh, especially in the regions of the dynodes. The user created mesh, denoted as *Custom* in figure 5.3.1, shows the smallest deviations from the reference mesh when the whole PMT geometry is evaluated and further improves over the *Extra Fine* mesh for the regions of the dynodes. These regions are the main interest, as the "Total" selection contains points where the electrons will not be propagating through. The main advantage of the *Custom* mesh is that it requires much less memory as well as solving time as the *Extremely Fine* mesh while only deviating slightly from it in the regions of interest.

5.3.2 Energy conservation

First, the energy conservation of the above mentioned meshes is compared. This is done with the procedure explained in section 5.2 for all four meshes. The result is depicted in figure 5.3.2 where the colorbar indicates the change in gain. A blue color indicates a smaller than expected gain while a red color indicates a higher than expected gain. A white color indicates no change in gain. The labels on the x-axis correspond to the dynodes in the multiplication system.

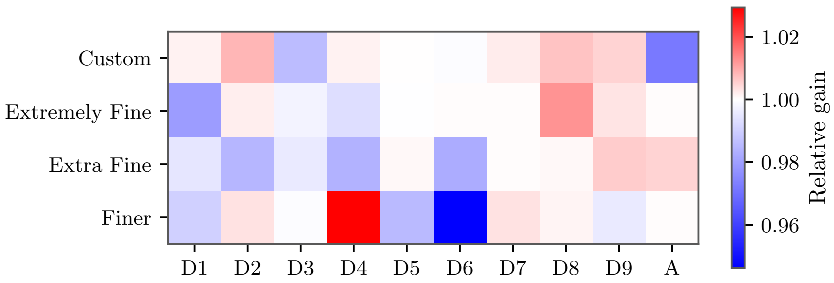

Figure 5.3.2: Comparison of the energy conservation for the four different meshes. The colorbar indicates the relative Gain calculated from the energy conservation.

It is observed that for all meshes the relative gain fluctuates to both positive and negative values. The extreme values are located with the *Finer* mesh in the fourth (highest value) and sixth (lowest value) dynode. It is also important to note that the range of the lower relative gain values is larger than for positive relative gain. To compare the total expected change in gain of the meshes the product of the relative gain over all dynodes is taken. This results in the over all change in gain listed in table 5.3.2.

From these values the results of the *Finer* and *Extra Fine* mesh are comparable while the *Custom* mesh is similar to the *Extremely Fine* mesh. The behaviour of the *Extra Fine* mesh is surprising since it showed better accuracy in the comparison of the electric fields in section 5.3.1. The similar result for the *Custom* and *Extremely Fine* mesh is beneficial when also considering the difference in runtime between the meshes.

Table 5.3.2: Obtained values for the relative gain across the full multiplication system for the four different meshes.

Mesh	Total change in Gain
Finer	0.95
Extra Fine	0.95
Extremely Fine	0.99
Custom	0.98

5.3.3 Time accuracy

The time accuracy of the simulation can be probed using the energy conservation, as explained in section 5.2. This is done for the four meshes presented above resulting in figure 5.3.3. Here the colorbar indicates the absolute time difference of the time of flight of the particles due to energy conservation. A blue color corresponds to a lower time while a red color indicates higher time. White corresponds to no change in the timing parameters. The labels on the x-axis correspond to the dynodes in the multiplication system.

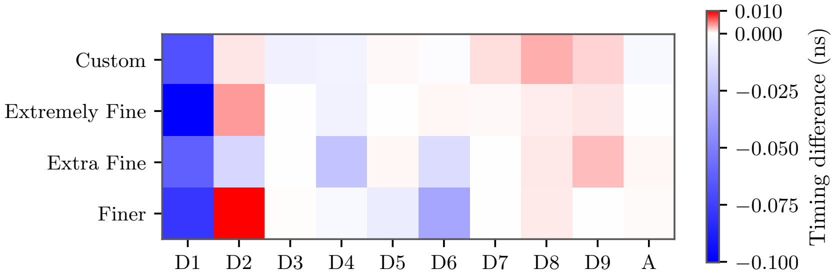

Figure 5.3.3: Comparison of the timing accuracy of the four meshes. The colorbar shows the timing difference calculated from the energy conservation. Note that the scale is different for positive and negative direction.

It is apparent that the timing accuracy of the first dynode shows significantly larger differences then the rest of the multiplication system. A clear reason for this behaviour is not known. One potential bias of this value is the amount of time steps used to calculate the trajectory, as more time steps naturally lead to a higher value. The number of time steps of the first four dynodes, however, are around 3000 depending on the mesh. At the latter stages this decreases to about 1000 time steps. Also to consider is the propagation distance done with each time step. As the distance from the photocathode to the first dynode is about three times larger than that from the first to the second dynode, this means that the trajectory length per time step is also larger, possibly inducing these higher deviations. Further investigation into this topic is necessary though.

Surprisingly, the *Extremely Fine* mesh has the highest deviation for the first dynode of about -0.1 ns. The rest of the multiplication system has much smaller values, being between one and three orders of magnitude smaller than the value at the first dynode. Note that the scale of the colorbar in figure 5.3.3 is not symmetric. To get an impression of the total timing accuracy of the meshes the sum over all timing differences is calculated. This way, fluctuations in both directions can cancel each other out. The values can be read in table 5.3.3.

The *Finer* and *Extra Fine* mesh are comparable within the order of ps. The *Extremely Fine* mesh is better than both of them, introducing a total timing difference of -0.1 ns. Surprisingly, the user created *Custom* mesh surpasses the *Extremely Fine* mesh, yielding only a

Table 5.3.3: Obtained values for the timing difference across the full multiplication system for the four different meshes.

Mesh	Total timing difference
Finer	$-0.114\,\mathrm{ns}$
Extra Finer	$-0.112\,\mathrm{ns}$
Extremely Finer	$-0.100\,\mathrm{ns}$
Custom	$-0.075\,\mathrm{ns}$

$-0.075\,\mathrm{ns}$ total timing difference across the full multiplication system. A reason for this behaviour is not known but it indicates that the validity of the simulation as well as the system resource requirements can be improved by further improving the mesh.

5.4 Influence of solver settings

There are several parameters in the algorithms used for the simulation and sampling all of these parameters goes beyond the scope of this thesis regarding the time to explore and detail to explain all parameters sufficiently. One parameter that stands out and will be addressed here is the time stepping.

As mentioned in section 4.2.4 the generalized-alpha time stepping scheme is used. This algorithm itself has a lot of parameters to investigate of which a constraint on the maximum time step is probed. This is the largest time step the solver can take during the computation of the *time dependent* study. In principle, the accuracy of the solver should improve with shorter time steps. In order to asses the impact of this effect the *Finer* mesh is used, which showed the worst performance out of the tested meshes. The distribution of the solver step sizes is shown in figure 5.4.1 to obtain a sense of their magnitude. In this example the maximum step size constraint is set to $1\,\mathrm{ns}$.

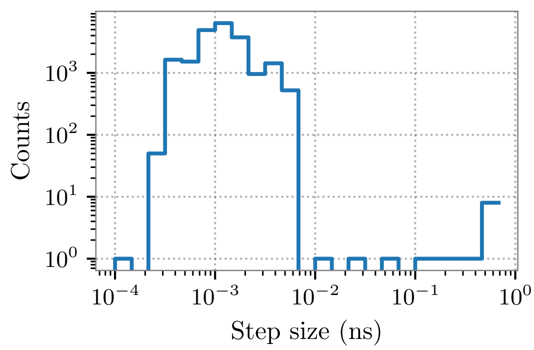

Figure 5.4.1: Distribution of the step size taken by the solver for the *time dependent* study. The constraint for the maximum step size is $1\,\mathrm{ns}$.

It becomes clear that the majority of the step sizes are well below this constraint ranging from two to four orders of magnitude. The few steps with step sizes close to $1\,\mathrm{ns}$ occur at the end of the solving process [30] when all the particles have hit a boundary and are frozen.[31] Therefore, no more propagation is done and the solver increases the step size to save system resources. This needs to be kept in mind when adjusting the simulation setting.

[30] This can be seen in the solver log file.

[31] Frozen meaning that the properties of the particle are constant for the rest of the simulation and no force can act on them anymore.

5.4.1 Energy conservation and timing accuracy

First, the energy conservation and its impact on the gain and timing accuracy for the simulation is considered. The results of this depicted are shown in figure 5.4.2a and figure 5.4.2b for the relative change in the gain and the timing difference respectively. Note that the value for the maximum time step of $0.0005\,\mathrm{ns}$ saturates the colorbar for the first dynode (denoted D1).

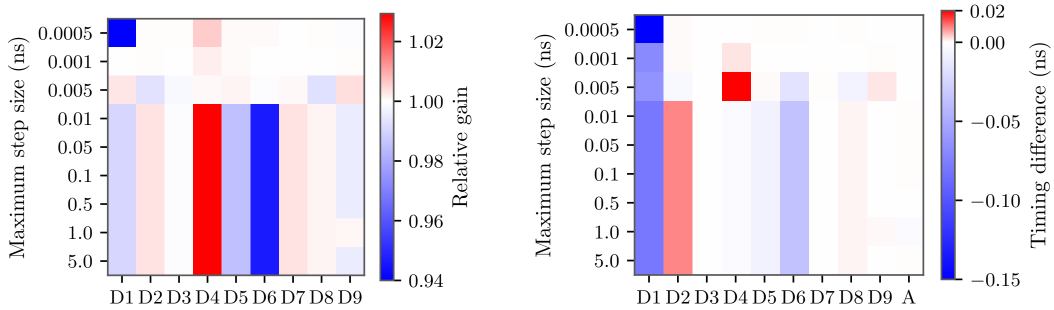

(a) Energy conservation. **(b)** Time accuracy.

Figure 5.4.2: Relative gain and timing accuracy of the solver for different values of the maximum time step size. Figure 5.4.2a shows the change of the relative gain while figure 5.4.2b shows the difference in timing calculated from the energy conservation.

The accuracy of the solver does not change when reducing the maximum time step size of the solver until a value of $0.005\,\mathrm{ns}$. This is expected from the distribution of time steps shown in figure 5.4.1. One important note is the result for $1\,\mathrm{ns}$ maximum time steps in the ninth dynode and the anode. Here the values change slightly. The reason for this behaviour is not known, especially as the solver does not change when using other time step constraints.

When the maximum time step is lowered to $0.001\,\mathrm{ns}$ the highest solver accuracy is obtained. Lowering the value further surprisingly decreases the accuracy dramatically. The reason for this behaviour is unknown and counter-intuitive as one would expect the accuracy to increase when more steps are taken. Since this behaviour is present in both the relative gain the the timing difference it seems to originate from the simulation and not from the way these metrics are calculated. It could be a feature of the solving algorithm, where the error estimation that is done to obtain the next time step is not working properly for these extremely small time steps.

The result from all dynodes can again be combined into a total result for the simulation. The values for the relative gain are multiplied to obtain the total change of the gain due to the energy conservation. The total timing difference is calculated by surmising all dynodes and the anode. The final results are listed in table 5.4.1. Note that not all investigated time constraints are shown as some are identical.

The result for the largest two time steps are similar with the gain being lower by about $5\,\%$ and the timing $-0.12\,\mathrm{ns}$. Lowering the constraint for the maximum time step size by three orders of magnitude improves the accuracy of the solver significantly. The solver impact on the gain in this case is below $1\,\%$ and the timing difference smaller than $-0.1\,\mathrm{ns}$. Lowering the time step size further to $0.0005\,\mathrm{ns}$ yields much worse values. This behaviour is again unexplained. Further lowering the maximum step size constraint is not possible as this exceeds the capabilities of the python package to export the data. Table 5.4.1 additionally contains the time needed to perform the simulation. This increases with a decreasing value for the maximum time step size as expected. It is important to note that this simulation is done

Table 5.4.1: Accuracy of the solver for different values of the maximum time step size. The values are obtained by combining the results from figure 5.4.2a multiplicative for the change in gain and figure 5.4.2b additive for the total timing difference. Additionally, the solving time of the *time dependent* study is listed.

Max. time step (ns)	Change in Gain	Total timing difference (ns)	Runtime (min)
5	0.953	−0.11	6
1	0.946	−0.12	6
0.005	0.993	−0.06	9
0.001	1.003	−0.06	17
0.0005	0.892	−1.07	37

for very few particles only and the time does not necessarily scale linear with the number of particles. This value also heavily depends on the hardware used for the computation.[32]

5.4.2 Position

Since this analysis only uses one mesh the position of the particles can also be investigated and compared between the different maximum time steps. The final position of the particles is displayed in figure 5.4.3 for the first four dynode, the ninth dynode and the anode. Note that the y-axis of the plot shows the y- or z-position of the respective dynodes depending on where the deviations are larger. This is due to the correlation between these two directions arising from the PMT symmetry in the y-z-plane and the orientation of the dynode. The x-axis always shows the x-position.

The final position of the particle on the first three dynodes changes by a few $0.01\,\mathrm{mm}$ in either direction across all maximum time step constraints. This change also only occurs for step sizes smaller than $0.005\,\mathrm{ns}$ as larger values essentially result in the exact same simulation. The change in position increases to a few $0.1\,\mathrm{mm}$ in the rest of the multiplication system with the y-position on the ninth dynode changing above $1\,\mathrm{mm}$. A slight deviation of the final position for $1\,\mathrm{ns}$ step sizes can also be seen for the last two dynodes. This is unexpected as the simulation should remain the same for this region of maximum time steps. This change also explains the deviation observed in the previous chapter.

As there is no true value known for the position of the particles and no clear pattern can be observed, no interpretation about whether one time step constraint is favourable above the others is done.

[32]For this analysis 18 cores of an Intel Xeon Gold 6140 CPU equipped with $80\,\mathrm{GB}$ of RAM are used.

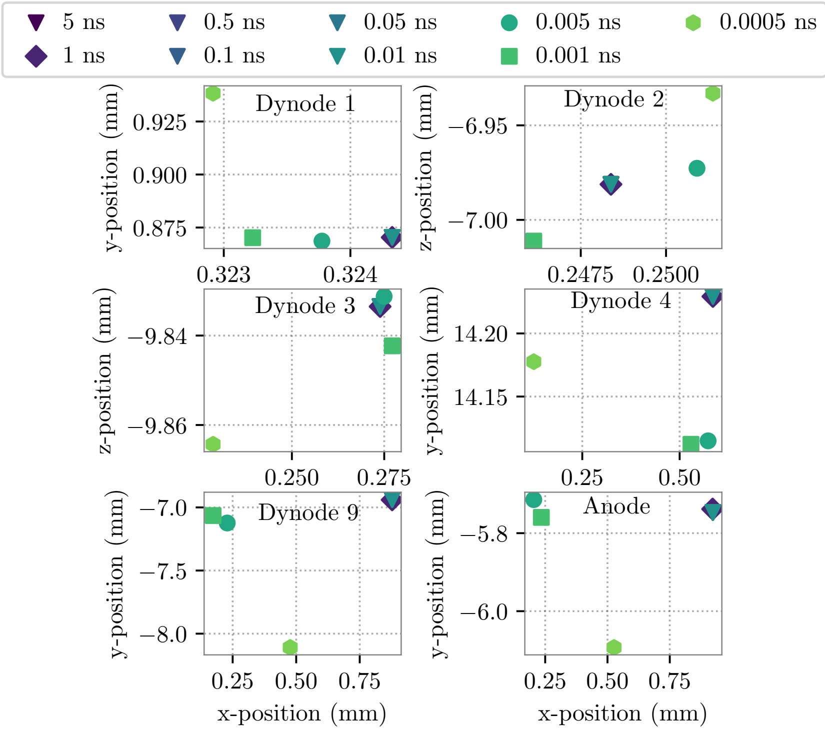

Figure 5.4.3: Final position of the particles for different maximum time steps. The upper left plot shows the first dynode, the upper right the second dynode, the center left the third dynode, the center right the fourth dynode, the lower left the ninth dynode and the lower right the anode. Note that the y-axis is different between the plots.

5.5 Combined simulation accuracy

In this section the accuracy of the simulation is presented and compared to some properties of a real mDOM PMT. For this, the testing methodology described above is repeated with the initial conditions described in section 4.2.3 applied to the photoelectrons. The initial position is chosen to be distributed equally across the photocathode area. The user created *Custom* mesh is employed as it showed good results in relation to the system resources needed. The maximum time step is set to 1 ns. In principle the accuracy could be increased by selecting a smaller value, however, the investigation of this parameter is not conclusive as the accuracy of the lowest value is the worst over all. Therefore, it will remain unchanged but further investigations into this could improve the simulation accurary.

5.5.1 Impact on gain

To see the impact of the simulation on the theoretical gain of the PMT the procedure described in section 5.2 is used. The energy conservation along the trajectory is calculated and the distribution of the change of the gain shown in figure 5.5.1. The blue dots represent the result for individual particles and the orange triangles the mean value of all particles for the specific dynodes. The total value is calculated by multiplying over all mean values.

The fluctuations in the gain are below 1 % for all dynodes except the second. This could be due to the high field gradient the particles experience, when propagating from the first to the second dynode due to the close proximity of their trajectory to the third dynode. Similarly, the spread of the fourth dynode is larger than the following dynodes.

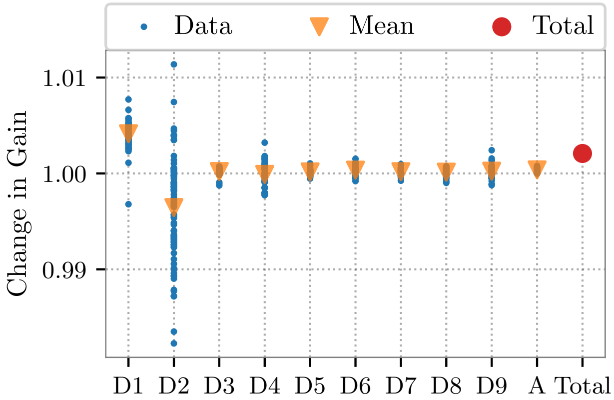

Figure 5.5.1: Theoretical change in PMT gain calculated from the energy conservation of the simulation. The blue dots represent the different particles while the orange triangles show the mean value for the respective dynodes. The last value shows the product over all mean values giving the mean total change in gain.

The total change in gain for the simulation is calculated to be 1.002 and very close to unity. It needs to be kept in mind that the assumption of the exponent in equation (5.2.1) being $\beta = 1$ is conservative so the actual effect should be smaller than the calculated value.

When the gain of a PMT is calibrated in actual measurements, the charge spectrum is fitted by the sum of several Gaussian distributions [52]. The mean value of the Gaussian corresponding to the spectrum of one photoelectron is then the gain of the PMT. The variance between pulses is expressed by the variance of the fitted charge distribution. A typical value for the *charge-resolution* is in the region of about $40\,\%$ [22]. Comparing this with the simulation impact on the gain it is safe to assume that the theoretical gain fluctuation imposed by the energy conservation of the simulation would not alter the result of the gain of the PMT should it be simulated.

5.5.2 Timing accuracy

The timing accuracy of the simulation is also calculated from the energy conservation. The calculated values are illustrated in figure 5.5.2 with the blue dots representing the individual particles and the orange triangles the mean value over all particles for the particular dynode. The total value is calculated by adding all mean values together.

The largest time difference is introduced by the first dynode, being at least an order of magnitude larger than the following dynodes. The second dynode also has a significantly larger contribution compared to the rest of the multiplication system. The remaining dynodes are accurate within $\pm 0.001\,\mathrm{ns}$.

The total timing accuracy is calculated to be $-0.336\,\mathrm{ns}$ which is dominated by the contribution of the first dynode. Actual measurements of the TTS of an mDOM PMT show that it is in the region of $2\,\mathrm{ns}$ [22] [33] meaning that the contribution of the simulation is large enough that it should be considered when interpreting the timing properties of PMTs through the simulation.

[33] This varies between PMTs and the way the measurement and analysis are performed.

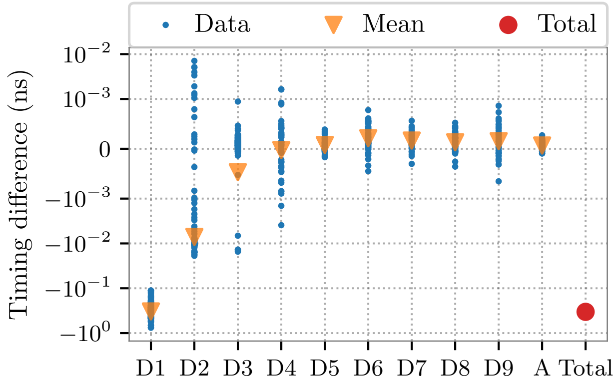

Figure 5.5.2: Time difference of the simulation calculated from the energy conservation of the simulation. The blue dots represent the different particles while the orange triangles show the mean value for the respective dynodes. The total time difference is the sum over the mean value of all dynodes.

5.5.3 Particle deletion at third dynode

As mentioned in section 4.4 there are two geometries used during the creation of the simulation. The initial geometry was replaced as the particle propagation did not go beyond the third dynode. The current hypothesis for this is that the attracting field of the third dynode (the field strength from second to third) is similar in magnitude as that of the fourth dynode (field strength from third to fourth). This results in the electrons being pushed back into the third dynode and subsequently being deleted from the simulation by COMSOL to save system resources. While it is possible to impact this deletion process, it results in instabilities and is therefore not done.

This deletion process is still present in the geometry reconstructed from a CT scan and results in difficulties for the data analysis. The extend of this effect is demonstrated in figure 5.5.3 were 1000 electrons are generated at rest on the surface of the third dynode.

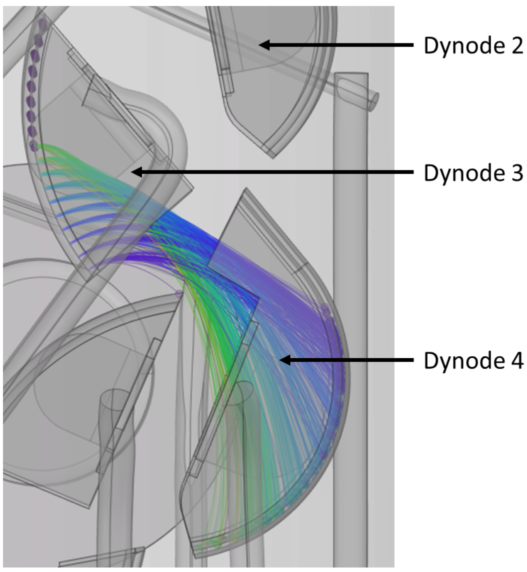

Figure 5.5.3: Simulation error at the third dynode. The lines represent the particle trajectories while the dots represent their initial and final position.

It becomes clear that particles which hit the third dynode in the upper part are not accelerated towards the fourth dynode. This poses several problems for the upcoming analysis of the simulated data.

First, when looking at the collection efficiency of the PMT a large systematic error is introduced as only about $55\,\%$ of the starting particles arrive at the fourth dynode so this effect needs to be considered when investigating the collection efficiency of the PMT. Additionally, these particles would increase the collection efficiency of the third dynode. This can be compensated to a certain degree by only analyzing particles that have a time of flight larger than a certain threshold. This way the secondary particles that are generated in the upper part will not contribute to the results for the third dynode. In this example this amounts to about $26\,\%$ of the particles. The remaining $19\,\%$ of the electrons are deleted without ever moving from their position. These ratios can, however, not be used to correct the collection efficiency since it heavily depends on the position of the particle. Secondly, there is the impact on the timing properties. Particles that are released from a higher point on the third dynode need to pass a larger distance to get to the fourth dynode having a higher time of flight. As they are deleted by COMSOL this changes the distribution of the arrival time and time of flight in the simulation. A quantification of the impact of this effect is not possible as their trajectories are not known.

6 Analysis of simulation results

In this chapter the results of the simulation efforts are presented and analyzed. This is split into two parts for the different PMT illumination patterns described in section 4.2.3. First the illumination of a single spot on the photocathode is investigated (see section 6.1) followed by the illumination of the whole surface (see section 6.2). The results for both analyses are compared to measurements of an mDOM PMT. Contrary to the previous chapter the particle information is only exported for the last time step in the simulation. Therefore, the information about the full trajectory is not available as well as the initial position of the secondary particles. The latter limitation will be partially circumvented in chapter 7 where individual spots on the photocathode are investigated.

6.1 Electron emission at photocathode center

The result of the simulation for the point like illumination is shown in figure 6.1.1. In total 50000 particles are simulated. The figure, however, shows the simulation of 5000 particles as this is the visualization limit of the machine used for this work.[34]

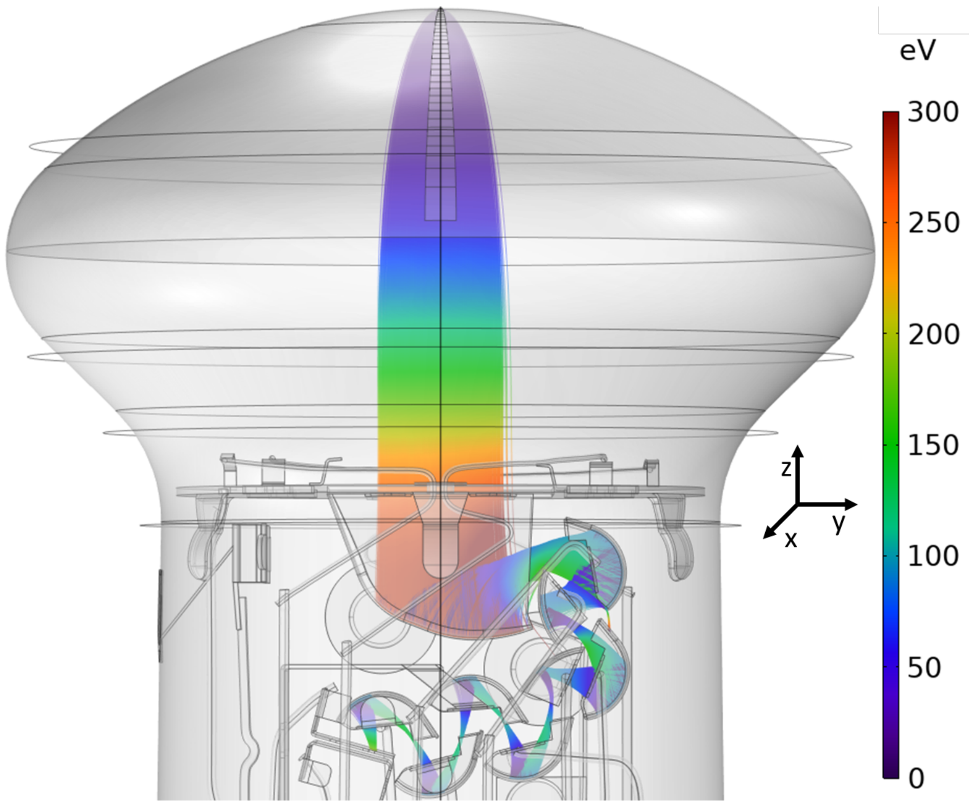

Figure 6.1.1: Visualization of the simulation of 5000 photoelectrons starting from a single point on the photocathode. The colorbar indicates the current particle energy. The rectangles on the photocathode area are related to the analysis in chapter 7.

[34]The COMSOL file for this simulation is about 90 GB in disk size.

The particles are released in a cone like shape and move through the multiplication system like expected. The beam of particles is rather wide while propagating towards the first dynodes but is focused significantly in the multiplication system. This is expected as the secondary particles do not have proper initial conditions applied and therefore, propagate according to the electric field only.

In the following sections the properties of the particles throughout the dynode system are investigated. First, a look at the collection efficiency is taken, followed by the introduction of the timing parameters. Lastly the wavelength dependence of some parameters is discussed.

6.1.1 Collection efficiency

The collection efficiency (CE) plays an important role in the multiplication process of any PMT. If at any point electrons are lost, then the signal strength is weakened. This is especially true for the earlier stages of the multiplication process as a loss in particles will multiply accordingly.

The CE is determined by simply counting the number of particles that arrive at a given dynode and comparing this value with a reference. This reference could be the amount of photoelectrons or the amount of particles at the previous stage. The first will give an impression of the absolute CE while the latter will show the relative CE between the different stages. Note that the latter value can be above $100\,\%$ when electrons hit different dynodes then intended. Both of these references will be used to give an impression about the CE of the PMT in the simulation. They are depicted in figure 6.1.2a where the blue dots correspond to the CE with respect to the previous multiplication step and the orange triangles correspond to the CE with respect to the number of photoelectrons starting from the photocathode. Additionally a close up of the visualization for the second to fifth dynode is given in figure 6.1.2b to better explain the observed data.

The CE of the first dynode is $99.99\,\%$, meaning that almost all released photoelectrons hit the first dynode. In figure 6.1.2b one electron is shown that does not hit the first dynode but instead is stopped on the back of the fifth dynode. A small fraction of electrons with the

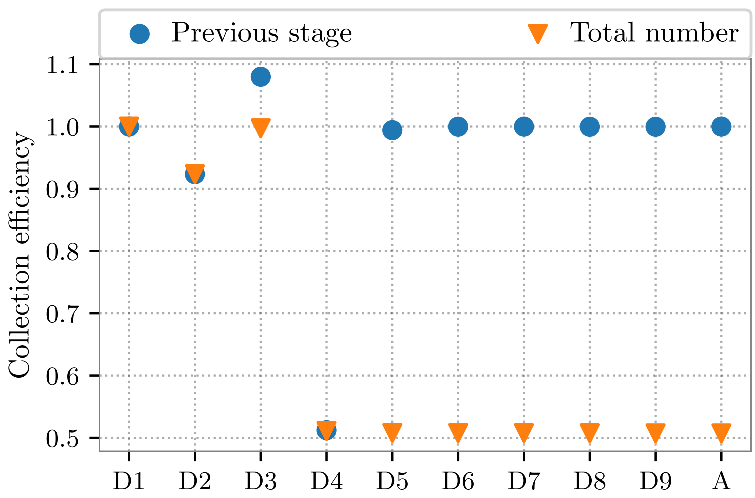

(a) Collection efficiency.

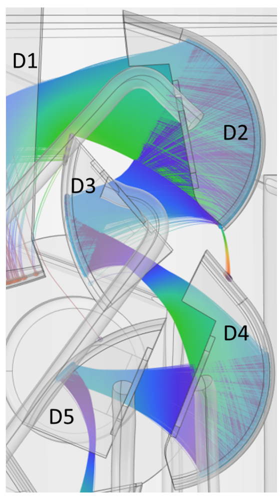

(b) Close up.

Figure 6.1.2: Collection efficiency of the PMT calculated from the simulation results in figure 6.1.2a. The legend corresponds to the reference used for the calculation. Magnification of the trajectories of electrons in the region of interest in figure 6.1.2b.

according release angle from the photocathode will take this path and thus will not contribute to the PMT response, lowering the CE of the first dynode.

The CE of the second dynode is significantly lowered to $92.3\,\%$. This is due to electrons hitting the third dynode from behind when they should propagate towards the second dynode. In figure 6.1.2b also some electrons can be seen that miss the second dynode and hit the back of the fourth dynode, lowering the CE further.

Consequently, the CE of the third dynode is higher at $107.99\,\%$ from electrons hitting the back side of it. Since the relative CE of the third dynode is calculated with respect to the number of electrons that hit the second dynode, the electrons missing from the second dynode due to hitting the third dynodes back are counted double. Additionally to the electron hitting the third dynode from behind, there are also electrons that get deleted here by the mechanism explained in section 4.4 and section 5.5.3. The secondaries that these electrons would generate are excluded from the analysis by applying a cutoff on the time of flight of each electron.

This deletion process also contributes heavily to the poor performance of the fourth dynode. Here, only $51.2\,\%$ of the electrons arrive. It is not possible to exactly quantify the contribution of the deletion as the trajectories of the deleted particles are simply not known. It can, however, be hypothesized that these particles would have trajectories with close proximity to the fifth dynode where some particles could hit the back and lower the CE similarly to what is happening between the first and second dynode. Additionally, the particles that hit the third dynodes back are also considered here. As those do not propagate towards the fourth dynode the CE is reduced further.

The rest of the multiplication system shows good performance regarding CE with almost all electrons arriving at the next stages (mean CE of these dynodes is $99.99\,\%$) The absolute CE mirrors this behaviour. It needs to be kept in mind that the secondary particles do not have proper initial conditions. It is expected that the CE will change should initial conditions be assumed as the spread of trajectories should increase. The impact of multiple starting positions from the photocathode on the CE is studied in section 6.2.1.

6.1.2 Timing parameters

For each particle two values are known regarding the time. First, the stop time is known which is the time when the propagation is stopped due to the particle hitting a boundary and subsequently being frozen in time until the simulation finishes. Secondly, the time of the particles creation, or the release time, is known.

From the first value one can obtain the arrival time, or transit time (TT), of the particles with respect to the emission from the photocathode. If the second value is taken into account, it is possible to calculate the time of flight of each particle. This would be the transit time of the particles between the different multiplication stages.

The distribution of the arrival times for the first four dynodes and the anode is depicted in figure 6.1.3a. The remaining dynodes are not shown in the figure since the distributions shape is mostly retained after the fourth dynode and to improve the readability of the plot.[35]

The arrival times on the first dynode are narrower distributed than those of the latter stages. Presented in figure 6.1.3b is the standard deviation of the distribution of trajectory lengths of the particles for all dynodes. The spread of the first dynode is about four times smaller than that of the second dynode. In combination with the higher particle energy (about three times) this results in the narrower distribution of the arrival time for electrons arriving at the first dynode compared to the second, third and fourth.

[35]The full data is presented in figure 9.0.1.

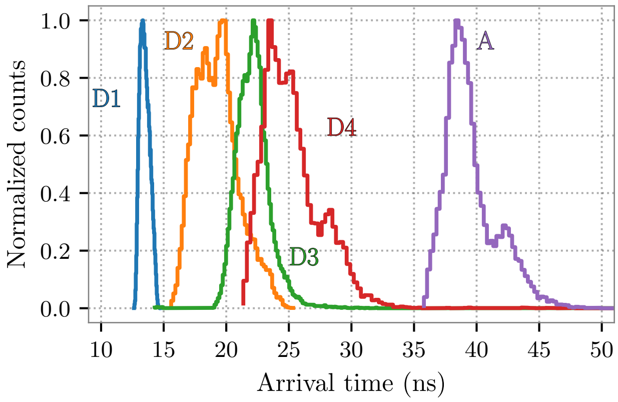

(a) Arrival time.

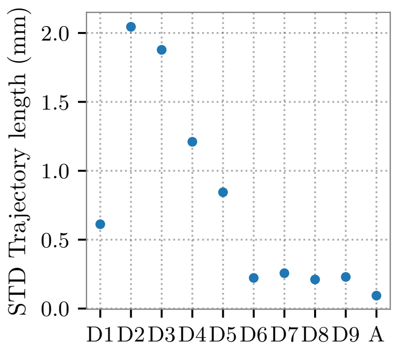

(b) Trajectory length.

Figure 6.1.3: Arrival times of the electrons for different dynodes. Shown in figure 6.1.3a is the signal at the first four dynodes and the anode. Figure 6.1.3b presents the standard deviation of the trajectory length between the multiplication stages.

Starting at the fourth dynode the arrival time distribution develops a second peak towards higher values which is consistent through the rest of the multiplication system. The exact origin of this second peak is unknown. As it only develops after the third dynode and is not found in actual PMT response measurements this is an error of the simulation and likely linked to the deletion process at the third dynode described in section 5.5.3. This process is believed to be due to poor resolution of the simulation of the electric field at the third dynode which leads to particles not propagating properly. This low resolution also leads to particles that do arrive at the fourth dynode to propagate very slow and on unusual paths when in the proximity of the third dynode like shown in figure 6.1.4.

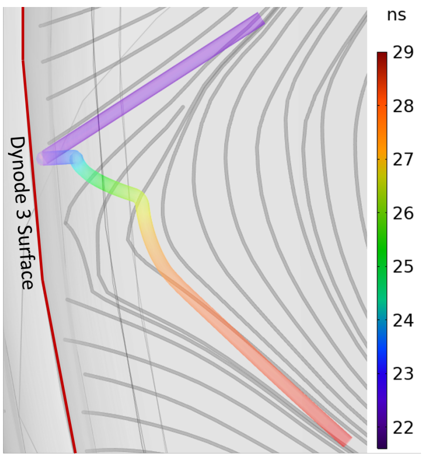

Figure 6.1.4: Example of the trajectory around the third dynode. The colorbar indicates the current time in the simulation. The blue tail is the incoming while the red tail shows the outgoing electron. The black lines indicate the electric field lines and the red line the dynode surface.

When looking at the colorbar it is clear that a large portion of the propagation time is spend in close proximity to the third dynode resulting in overall slowed particles. As theorized in section 6.1.1, the deleted particles would take paths that lead them to the lower part of the fourth dynode and possibly hit the back of the fifth dynode. As they would propagate a longer distance they would also have a later arrival time possibly masking the double peak shape of the distribution. The rest of the multiplication system is not shown except for the signal at the anode. Compared to the fourth dynode the shape is more uniform and narrower. The double peak feature is still present.

To compare the results of the simulation to measurements of the PMT timing parameters, the mean value and the standard deviation of the distributions are extracted by fitting a Gaussian distribution to the data. In actual measurements this is done to the peak of the main pulses (see figure 3.2.2b) by only fitting to data within a certain time window. As the simulation does not incorporate different pulse types the fit is done to the full distribution. The results can be compared to the transit time (TT) and the transit time spread (TTS) of the PMT. It is important to note that usually the relative TT of a PMT is shown as the setup of the Münster working group does not allow for the measurements of the absolute TT. The resulting parameters of the fits are given in figure 6.1.5a where the arrival time of the electrons with respect to the release of the photoelectrons from the photocathode is taken. Figure 6.1.5b represents the result of the arrival time with respect to the release of the particle from the previous stage. The blue dots correspond to the mean value shown on the left y-axis and the orange triangles represent the standard deviation with the scale on the right y-axis.

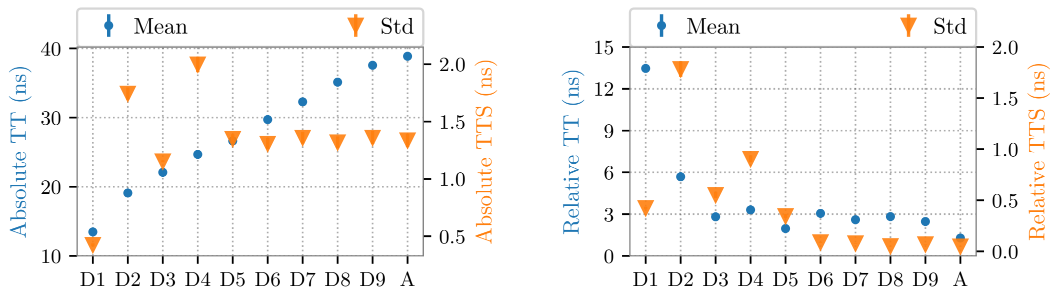

(a) Arrival time.

(b) Time of flight.

Figure 6.1.5: Timing parameters of the simulation of photoelectrons from a single spot on the photocathode extracted from the fit a Gaussian distribution. Figure 6.1.5a shows the values for the arrival times and figure 6.1.5b shows the values for the time of flight. The blue dots correspond to the mean value and the orange triangle to the standard deviation of a Gaussian fit which are interpreted as the transit time (TT) and transit time spread (TTS) respectively.

When first examining figure 6.1.5a the absolute TT of the PMT rises almost linearly with the different stages to a mean absolute TT at the anode of (38.86 ± 0.06) ns which is slightly smaller than the typical electron transit time given by the manufacturer of 43 ns obtained with a supply voltage of 1000 V [25].[36] The difference in absolute TT is expected when the supply voltage of 1200 V for the simulation is taken into consideration. A higher voltage results in greater acceleration and therefore, lower transit times are expected. Additionally, the tenth dynode does not contribute in the geometry of the simulation and the electrons propagate directly from the ninth dynode to the anode. The impact of this should be small as the distance between the tenth dynode and anode is small.

The absolute TTS increases from the first to the second dynode but decreases from the second to the third. The first increase can be explained by the larger amount of possible paths for the electrons. The electrons with a larger trajectory length land on the lower part of the second dynode and therefore have a shorter path towards the third dynode. This could explain the decrease of the TTS at the third dynode. In general, only in the first four multiplication

[36]This is for PMT model R12199 which has identical internal structure compared to the mDOM PMT R15458 only being inside a longer glass bulb.

stages have significant contributions to the TTS as it remains almost constant thereafter resulting in a final absolute TTS of (1.36 ± 0.06) ns at the anode. In actual measurements the TTS of an mDOM PMT is determined to be (1.11 ± 0.01) ns when only a single spot in the center of the photocathode is illuminated [22]. So the simulation overestimates the TTS by about $20\,\%$ which is possibly due to the second peak in the simulated data. When the TTS of the third dynode of (1.15 ± 0.01) ns is used for the comparison this difference shrinks to about $4\,\%$, resulting in a better agreement. It needs to be kept in mind that the properties of the PMT can vary due to the different voltages at which the characterization is performed. This is typically done at the nominal gain of $5 \cdot 10^6$ which corresponds to 1135 V for BA0784 which is used in this comparison [22].

Of interest is also the result shown in figure 6.1.5b, where the TT and TTS of the electrons with respect to their release times at the previous stage is shown. The relative and absolute TT for the first dynode are the same as is expected. The relative TT decreases to (5.68 ± 0.07) ns on the second dynode. After that the relative TT is (2.54 ± 0.05) ns on average, meaning that for stages past the second dynode the absolute TT rises linearly.

A similar behaviour is found in the relative TTS where the second dynode has the largest contribution of (1.78 ± 0.08) ns. This behavior is explained by the larger spread in the trajectory length for the second dynode. The contributions of the third, fourth and fifth dynode ((0.55 ± 0.03) ns, (0.91 ± 0.03) ns and (0.35 ± 0.02) ns respectively) are two to six times smaller than that of the second dynode. The rest of the dynode system has a mean relative TT of (0.066 ± 0.007) ns and is more than an order of magnitude smaller than the second dynode highlighting the well focused particle beam in these stages once again. It is again noteworthy that the secondary particles do not have proper initial conditions. With the implementation of those initial conditions it is expected that the relative TT and TTS of the latter dynode stages will have a more significant impact on the PMT properties.

6.1.3 Wavelength dependence of TTS

During the development of the mDOM for the IceCube Upgrade the PMTs are rigorously tested for their properties and stability in their destined environment. These tests include the dependency of the PMT timing performance on the wavelength where a strong relationship between the TTS and the wavelength of the photon was found [37]. This dependence is believed to be due to the initial spread of the starting directions of photoelectrons depending on the wavelength (see figure 6.1.1) and the initial particle tracing studies confirmed this hypothesis [50]. In these studies, however, only the path from the photocathode to the first dynode was examined. This was extended to the full multiplication system in this thesis.

The result of the simulation [37] is evaluated like described above and the standard deviation of the arrival times is extracted for different wavelengths, ranging from 350 nm to 650 nm. The simulated and measured data is presented in figure 6.1.6a where a linear fit is performed to both datasets. The blue dots represent the simulated data with the orange line for the fit while the red dots correspond to the measurement data with the green line for the fit.

The TTS in both the simulation and measurement is decreasing with increasing wavelength. The linear fits result in a slope for simulated data of (-0.31 ± 0.01) ns/100nm and measurement data of (-0.23 ± 0.01) ns/100nm. The slope of the simulation is about $35\,\%$ larger than that of the measurement. Additionally, the TTS of the simulation is slightly larger by about 0.25 ns depending on the wavelength. This difference is possibly due to the double peak behaviour of the arrival time at the anode which is presented in the previous section (see

[37] The number of photoelectrons for this analysis is reduced to 10000.

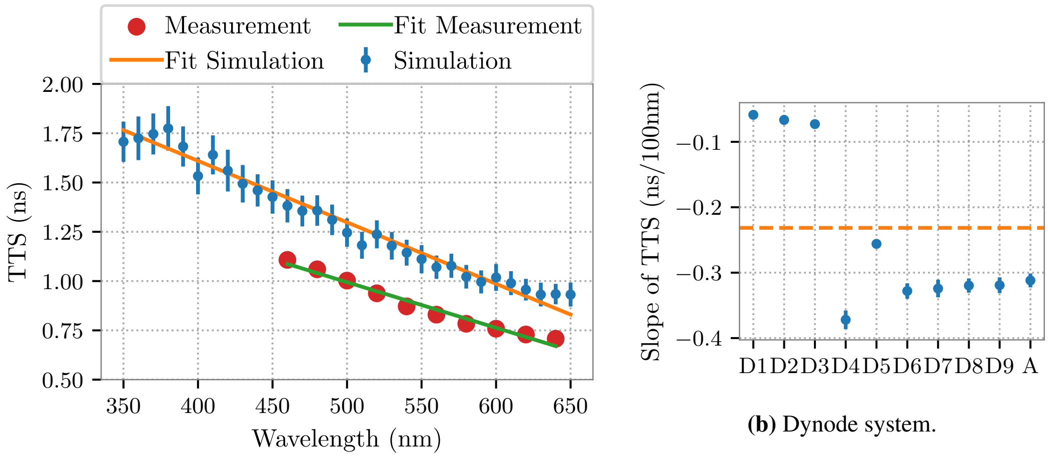

(a) Anode.

(b) Dynode system.

Figure 6.1.6: Transit time spread (TTS) of the electrons arriving at the anode with measurement data taken from [22] in figure 6.1.6a. A linear fit is performed to each dataset. The slope of each multiplication stage extracted from the simulated data in figure 6.1.6b. The horizontal line corresponds to the slope of measurement data.

section 6.1.2) or different supply voltages between the simulation and measurement.

In [37] the contribution of the dynode system to the TTS was believed to be constant, while in [50] a linear contribution of the dynodes is assumed. The complete system was not available in that work but is now accessible. By extracting the slope of the TTS dependence on the wavelength for the components, figure 6.1.6b is obtained where the blue dots represent the slopes of the different stages and the horizontal line that of the measurement.

The slope of the first three dynodes is smaller than the measurement. It seems to be increasing hinting towards a dependence between the multiplication system and the wavelength. This is possibly due to the spot size of the particle beam on the respective dynodes resulting in different trajectory lengths as will be shown later. At the fourth dynode the slope of the simulation is larger than that of the measurement and decreases towards the anode. The jump between the third and fourth dynode could be due to the deletion process described in section 5.5.3 in combination with the different spot size of the particle beam. From the simulation data a linear contribution of the rest of the multiplication system can not be confirmed.

In previous works [22] it is hypothesized that the dependence of the TTS on the wavelength arises from the higher initial spread that photoelectrons receive after emission from the photocathode. This would increase the particle beam width between the photocathode and the first dynode shown in figure 6.1.1. This hypothesis was first confirmed by initial particle tracing studies performed in [50]. To illustrate this feature the positions of the particles on the first dynode are examined. This is presented for $460\,\mathrm{nm}$ and $640\,\mathrm{nm}$ in figure 6.1.7a.

In the raw distribution it is visible that the lower wavelength, or higher photon energy, occupies a larger space on the first dynode. The shape of both distributions is not perfectly spherical and has some deviations. These could be a result of the sampling of the initial direction and energy done by COMSOL. The large amount of photoelectrons simulated should suppress this, though. The PMT geometry also should not induce this deviation either, especially as the PMT is symmetric in the x-direction. In the distribution of the final positions, however, there is a distinct asymmetry in the x-direction for $y \approx 4\,\mathrm{mm}$.

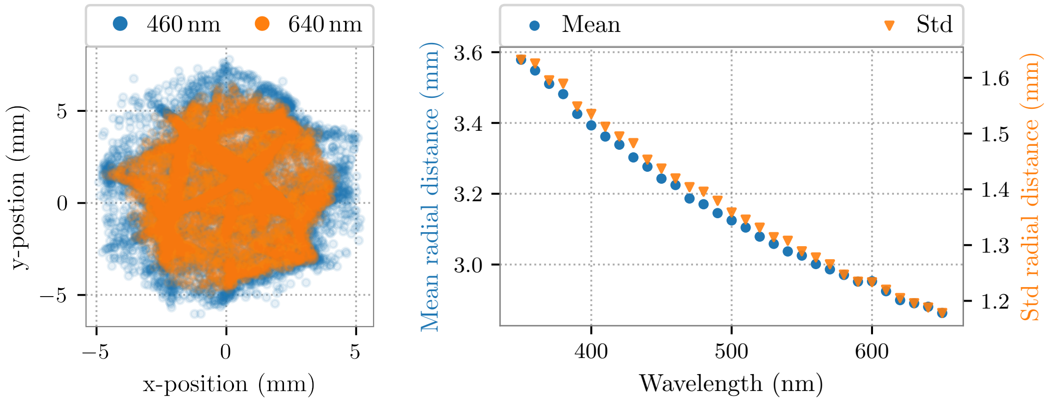

(a) Final position on first dynode. **(b)** Wavelength dependence.

Figure 6.1.7: Final position of the particles on the first dynode. Figure 6.1.7a shows the position for two wavelengths and figure 6.1.7b shows the mean value and standard deviation of the radial distance to the center. The z-position of the particles is not considered in either plot.

Calculating the radial distance from the PMTs center with $r = \sqrt{x^2 + y^2}$, the mean spot size and its standard deviation are calculated and shown in figure 6.1.7b. The z-coordinate is not considered here. Since the surface of the first dynode is mostly in the x-y-plane compared to the other dynode (see figure 6.1.1) the impact should be small. Both the mean spot size and its standard deviation decrease with increasing photon wavelengths. This strengthens the hypothesis about the origin of the wavelength dependence on TTS. As shown before, the rest of the multiplication system also contributed to this

6.2 Electron emission from photocathode surface

When the full photocathode area is illuminated, photoelectrons are liberated from the whole photocathode surface. This illumination pattern can also be simulated with COMSOL and an example of 5000 simulated photoelectrons is depicted in figure 6.2.1. For the following analysis 50000 photoelectrons are simulated and evaluated.

In the visualization of the simulation it can be observed that the paths of the photoelectrons converge towards the first dynode. Their spread is expectedly larger than that of the point like illumination in section 6.1. The particle beam is focused by the electric field similarly to the previously shown example and results in a well focused beam of particles after the fifth dynode.

6.2.1 Collection efficiency

The evaluation of the CE follows the same principle as described in section 6.1.1. Again the number of particles arriving at a certain stage are counted and then compared to a reference value (number of electrons at the previous stage or number of photoelectrons). The result of this analysis is presented in figure 6.2.2a with an enlarged portion of the multiplication system from the second to fifth dynode in figure 6.2.2b. The blue dots represent the CE with respect to the previous dynode and the orange triangles the absolute CE.

The results of this analysis are similar to that of the point like illumination pattern with differences mostly pronounced in the first three dynodes. The first dynode does not have the almost perfect CE as before, now collecting 97.2 % of the photoelectrons. As particles have more diverse starting positions, their trajectories can have closer proximity to the frontal plate

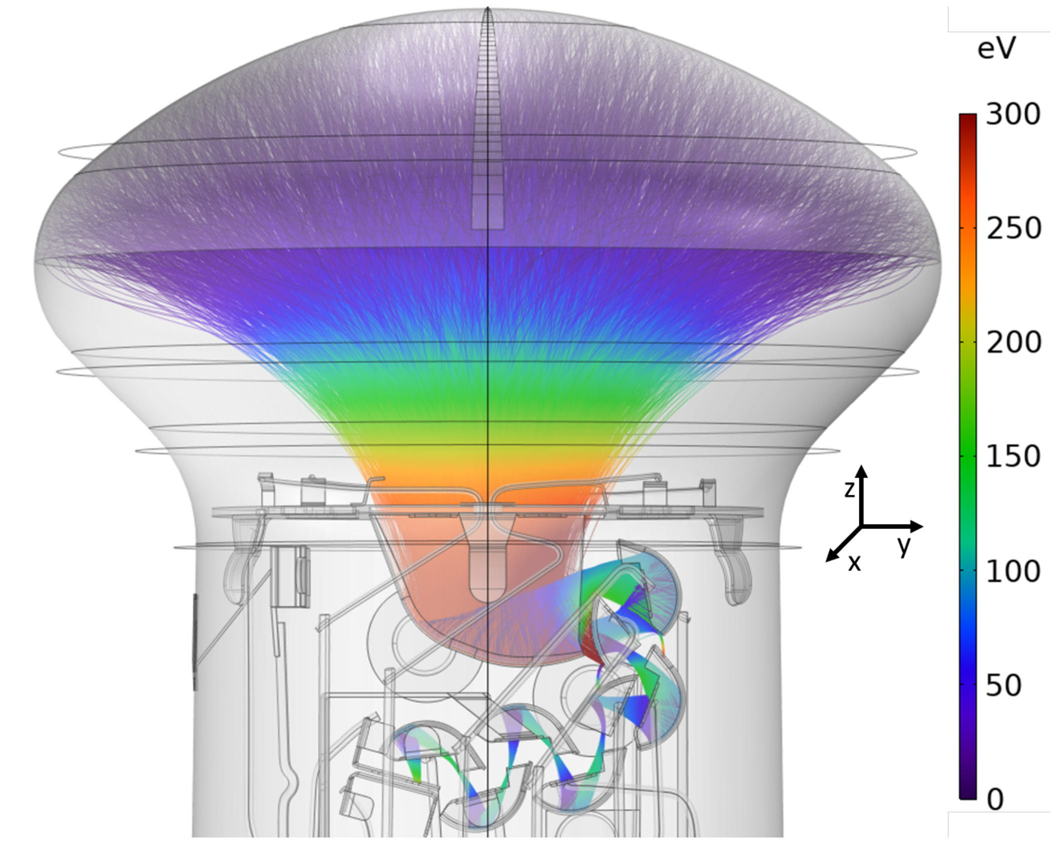

Figure 6.2.1: Visualization of the simulation of 5000 photoelectrons starting from the whole photocathode surface. The colorbar indicates the current particle energy. The rectangles on the photocathode surface are related to the analysis in chapter 7.

of the PMT. Electrons that are stopped on the frontal plate will not result in a PMT response and therefore lower the CE. This effect is not present in the simulation data, meaning that all released electrons are propagating inside the multiplication system. The CE deficit of the first dynode is explained by particles that miss the first dynode and hit the third dynode directly in the back. These would also not result in a PMT response as the back side of the dynode does not emit any secondary particles. This behaviour is also present for the release from a point but to substantially lesser degree as can be seen by comparing figure 6.1.2b and figure 6.2.2b. In total six particles miss the first dynode with the point release and 1420 for the surface release.

The CE of the second dynode is reduced with $87.2\,\%$ of the particles emitted from the first dynode being collected. This process is similar to that described in section 6.1.1 were particles hit the third dynode in the back while propagating towards the second dynode. The amount of these particle is higher as the initial positions on the first dynode are more spread. By comparing the CE of the second dynodes between the two illumination patterns this difference is about $5\,\%$. Similar to the point release, electrons arch over the third dynode, barely miss the second dynode and then hit the back of the upper part of the fourth dynode. These further reduce the CE of the second dynode as no multiplication occurs on this surface.

The photoelectrons that miss the first dynode and subsequently hit the back side of the third in combination with the particles propagating to the second dynode increase the CE of the third dynode to $115.8\,\%$. Note that the reference for this value is the amount of particles arriving at the second dynode. As this is already lowered a higher CE on the third dynode is expected similar to section 6.1.1.

Again, similar to the point like illumination pattern, the fourth dynode has a strongly

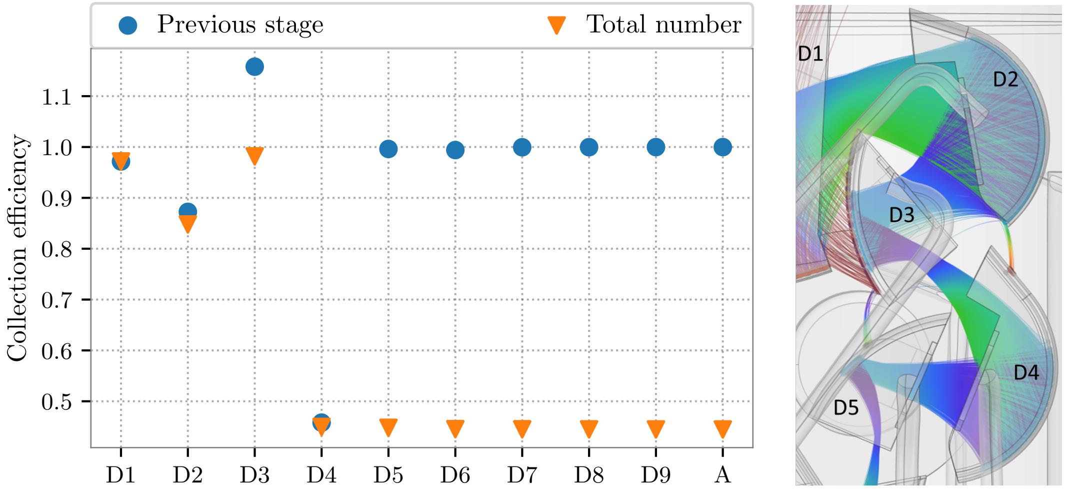

(a) Collection efficiency.

(b) Close up.

Figure 6.2.2: Collection efficiency of the PMT calculated from the simulation results in figure 6.2.2a. The legend corresponds to the reference used for the calculation. A magnified portion of the multiplication system in figure 6.2.2b to enhance the visibility of the trajectories of the electrons in the region of interest.

reduced CE of $45.8\,\%$ which is likely due to the deletion process at the third dynode described in section 5.5.3. This is an error in the simulation which can not be corrected easily. It can be hypothesized that these particles could hit the back of the fifth dynode would the propagation work properly. The rest of the multiplication system behaves identical to what is shown in section 6.1.1 with an average CE of $99.8\,\%$ showing the strong focus of the particle beam past the fourth dynode. It is expected that this will decrease, however, when proper initial conditions for the secondary electrons are introduced.

6.2.2 Timing parameters

Analogous to section 6.1.2, the timing parameters for the illumination of the whole photocathode surface are investigated with the above described procedure. Figure 6.2.3 contains the distributions of the arrival time for the first four dynodes and the anode.[38]

There are some clear differences between the distribution of the arrival time for the surface release and the point release. First, the distribution of the arrival times on the first dynode now has a shoulder towards higher values. This shoulder is also present in measurements of the mDOM PMT.[39] This features origin lies in the different starting positions which will be explored in more detail in chapter 7. The distribution of the third dynode shows a pronounced peak at earlier times which contains the electrons that propagate from the photocathode to the back of the third dynode.

The first thing to notice with the fourth dynode is the absence of the double peak feature, which developed for the point like illumination. As the deletion of particles is still happening (seen in the CE of the fourth dynode), this is possibly due to the shoulder of the distribution of arrival times on the first dynode. This would propagate through the multiplication system accordingly and mask the secondary peak which developed at the fourth dynode.

[38] The distribution of the other dynodes can be seen in figure 9.0.2.

[39] It is important to keep in mind that these measurements only contain the arrival time on the anode not the first dynode.

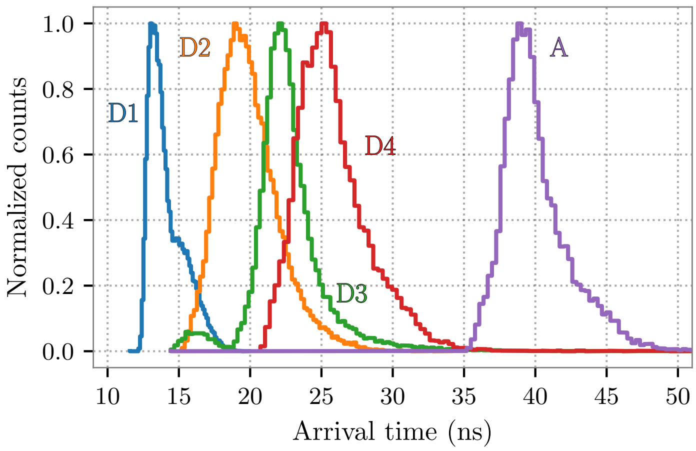

Figure 6.2.3: Distribution of arrival times of electron for different components. Shown is the signal at the first four dynodes and the anode.

The distributions are again fitted with a Gaussian function to extract the mean value and standard deviation acting as the TT and TTS respectively. The obtained values can be seen in figure 6.2.4a for the arrival time of the electrons at the different multiplication stages while figure 6.2.4b depicts those for the time of flight of the electrons between the stages. The blue dots correspond to the mean value on the left y-axis and the orange triangle to the standard deviation on the right y-axis.

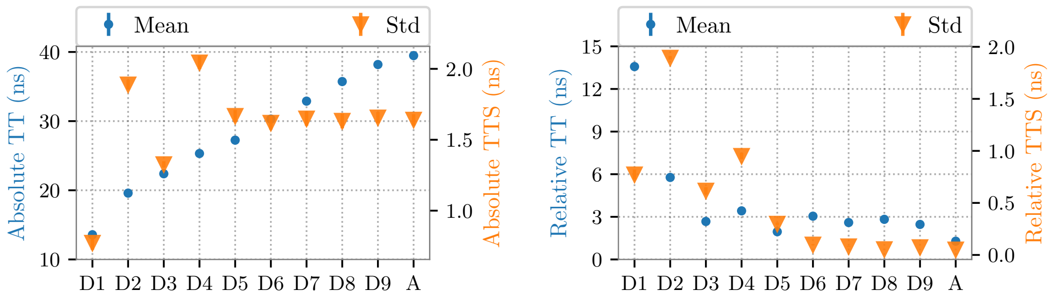

(a) Arrival time.

(b) Time of flight.

Figure 6.2.4: Timing parameters of the simulation for the surface release. Figure 6.2.4a shows the values for the arrival times and figure 6.2.4b shows the values for the time of flight. The blue dots represent the mean value and the orange triangles the standard deviation of a Gaussian fit.

In comparison to the previous result for the point like illumination the shape of the graph remains identical (see figure 6.1.5a and figure 6.1.5b). The difference between the two lies in the absolute values. The absolute TT to the anode of (39.48 ± 0.04) ns and the absolute TTS of (1.64 ± 0.04) ns are higher by $1.5\,\%$ and $22.3\,\%$ respectively compared to the previous analysis. This shows that the different starting position significantly increase the absolute TTS while the absolute TT remains similar to the point like illumination. A significant deviation in the absolute TT is not expected since the major difference between the two studies is between the photocathode and first dynode. This is reflected in the relative TT and TTS where the relative TTS of the first dynode of (0.77 ± 0.05) ns is (0.35 ± 0.05) ns larger than in the point like illumination. If this surplus would propagate through the multiplication system the absolute TTS at the anode would be $26.1\,\%$ larger. Since the increase in absolute TTS between the two illumination patterns is $3.8\,\%$ smaller than that, the remaining dynodes must reduce the spread. The main contributor to this is the fifth dynode where the relative TT of the surface release is $13.6\,\%$ smaller than that of the point release.

When the full photocathode surface is illuminated in measurements the TTS of the PMT is determined to be $(1.85 \pm 0.01)\,\mathrm{ns}$ [22] by fitting a Gaussian to the peak of the main pulses. There are fluctuations in TTS between different PMTs, explained by the different supply voltages used to achieve nominal gain. The absolute TTS obtained by the simulation is about $10\,\%$ lower than the measurement. This deviation could be due to the improper implementation of the secondary electrons. When proper initial conditions for these particles are applied, the TTS is expected to increase as the particle beam will be broader. Especially the contribution of the latter dynodes is expected to increase. Another deviation could be caused by different supply voltages as mentioned above. The typical TTS given from the manufacturer is $1.91\,\mathrm{ns}$ [25] [40] where a potential difference between the anode and photocathode of $1000\,\mathrm{V}$ is applied.

[40] This is for the PMT model R12199 which has the same internal components as the mDOM PMT (model R15458) but is housed inside a longer glass bulb.

7 Photocathode uniformity scans

The characterization of the mDOM PMTs for their deployment in the antarctic ice is done in bulk with the illumination of the full photocathode area. As presented in chapter 6, there is a difference in the properties of the PMT when illuminating the photocathode entirely or only spot wise. The same is true for measurements of actual PMTs. This lead to the investigation of the PMT properties in scans where a collimated light beam is used illuminating a single position on the photocathode in a grid like pattern. This chapter will introduce the scans of the photocathode which are performed to bypass the limitation of the data export and give more information about the positional dependencies of the PMT. They are a hybrid between the point and surface release where the photoelectrons are released from rectangular areas along the x- and y-direction of the photocathode. The rectangles are build in $1\,\mathrm{mm}$ steps in length and cover a width of $4°$ and the electrons are emitted uniformly from the surface. An example for this method is shown in figure 7.0.1 where 5000 photoelectrons are released from a position in negative y-direction ($y = -21\,\mathrm{mm}$).

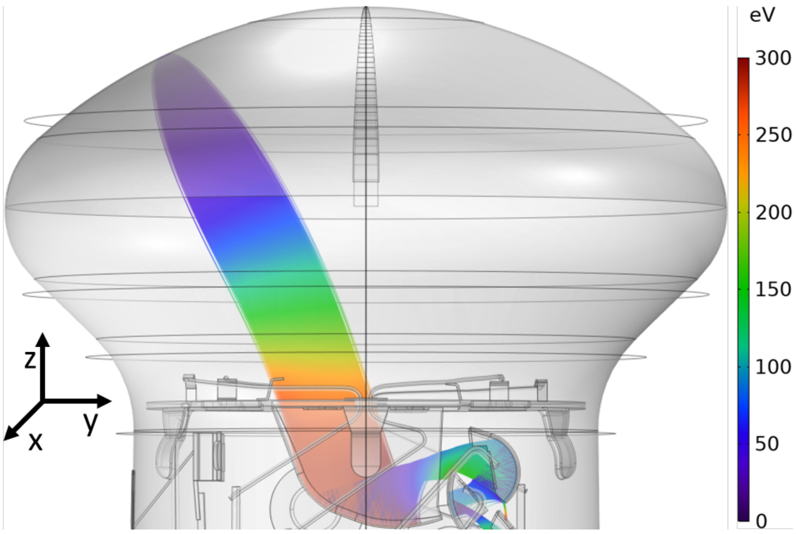

Figure 7.0.1: Example of simulation for the scan of the photocathode uniformity. The color indicates the particle energy.

For the analysis, each rectangle is set to emit 10000 photoelectrons. Their properties will be studied analogous to chapter 6. First, a look at the collection efficiency is done in section 7.1. Following this is section 7.2 with the investigation of the timing parameters and comparison to measurements of an actual mDOM PMT.

7.1 Collection efficiency

The collection efficiency (CE) is investigated with the number of photoelectrons as the reference. This is done as the CE with respect to the previous stage has some extremely high values especially at the outer edge of the PMT. As seen in section 6.1.1 and section 6.2.1, the CE of the later dynodes is close to $100\,\%$. For this reason, figure 7.1.1 only presents

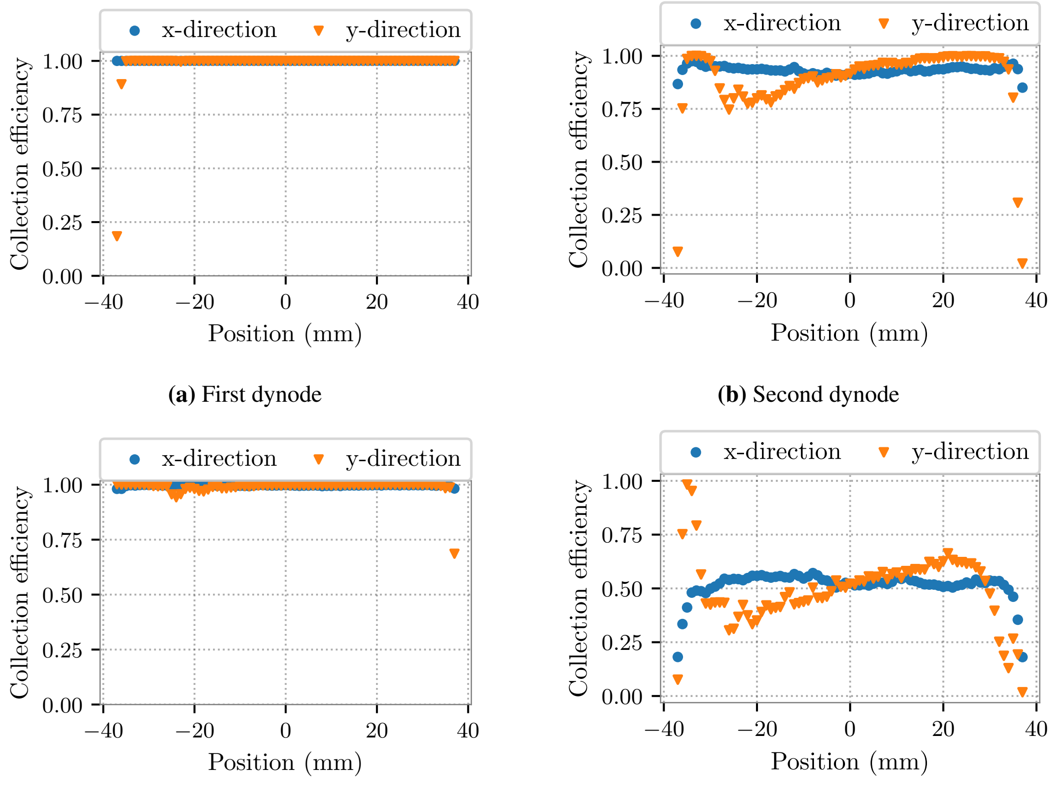

(a) First dynode

(b) Second dynode

(c) Third dynode

(d) Fourth dynode

Figure 7.1.1: Collection efficiency of the PMT along the x- (blue dots) and y-axis (orange triangles) with respect to the number of emitted photoelectrons for the first four dynodes.

the graphs for the first four dynodes with the blue dots representing the x-direction and the orange triangles the y-direction on the photocathode.[41]

At first glance it is visible that the CE along the x-direction is symmetrical around the PMT center throughout the dynodes which is to be expected from the design of the PMT. The CE of the first dynode is flat meaning that almost no electrons (CE $\geq 99.95\,\%$ for all positions) are lost by either hitting the frontal plate or the third dynode. On the second dynode the CE has a slight dip in the central region to $91\,\%$, similar to what is observed in section 6.1.1. This again is symmetric around the PMT center. Additionally, the CE of the second dynodes drops significantly for photoelectrons stemming from the edges of the PMT ($x^2 \geq 35\,\mathrm{mm}$) to about $85\,\%$. This is also present in the third dynode, though to a much lesser degree with $98.1\,\%$. Here the central region is flat again. The fourth dynode shows a small peak in the CE at around $-20\,\mathrm{mm}$. This behaviour is not shown on the positive side and its origin is not known. Further, the mean CE of the fourth dynode is only $51.3\,\%$ with even smaller values towards the edge of the photocathode. This behaviour is due to the deletion process at the third dynode (see section 5.5.3). All in all, the CE for the x-direction is almost constant in the central part of the PMT and decreases towards the edge. The general shape is symmetric around the center.

The y-direction on the other hand is asymmetric. This is first visible at the second dynode where the CE in y-direction declines from $0\,\mathrm{mm}$ to $-26\,\mathrm{mm}$ by about $25\,\%$. This decline is also present at the third dynode in a reduced scale. The CE of the fourth dynode is expected to be low considering the previous investigations (see section 6.1.1 and section 6.2.1). This

[41] The plots for the remaining dynodes can be found in figure 9.0.3.

holds for most positions with the exception for certain negative y-values around $-35\,\mathrm{mm}$. This would indicate that the particle beam for these positions hits the third dynode mostly in the lower part where the deletion process described in section 5.5.3 is not observed.

One downside of using the number of photoelectrons as the reference is that it is not immediately clear where the missing electrons might have gone. An example of this would be the lowest y-value on the first dynode ($y = -37\,\mathrm{mm}$) with a CE of only $18.4\,\%$. That of the second dynode in this position is also poor with less than $10\,\%$ of the initial photoelectrons arriving there. The third dynode, on the other hand, has an ideal CE, meaning that all $10\,000$ particles arrive there. This is due to the extreme angle at which the photoelectrons are emitted with respect to the first dynodes surface, resulting in most of them hitting the back of the third dynode. The CE of the fourth dynode is very poor again, as these particles can not propagate there. In principle the electrons hitting the third dynode in the back should not account for the CE since no secondary electrons are produced there. The final position on the first dynode of the photoelectrons for this starting position is visible in figure 7.1.2 with the orange dots. The hard cut in positive y-direction at $7.88\,\mathrm{mm}$ corresponds to the edge of the first dynode. Particles that would arrive above this would hit the back of the third dynode.

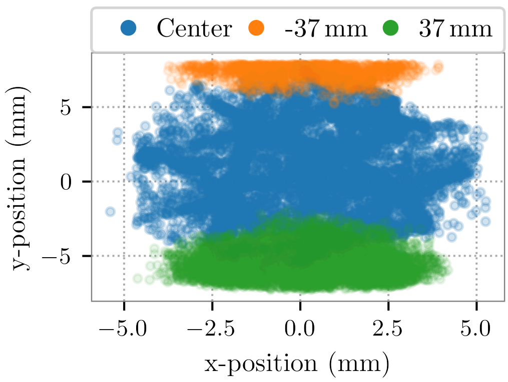

Figure 7.1.2: Final position of photoelectrons on the first dynode (2d-projection) from starting positions in the center, at $y = -37\,\mathrm{mm}$ and at $y = 37\,\mathrm{mm}$.

A second noteworthy feature is observable at the highest y-position on the photocathode ($y = 37\,\mathrm{mm}$). Here the CE of the first dynode is $100\,\%$, meaning all photoelectrons arrive on the first dynode. The CE of the following dynodes is lowered with the second and fourth dynode collecting around $2\,\%$ of the particles and the third dynode $68.6\,\%$. The electrons released from this location in the photocathode arrive at the positions on the first dynode presented in figure 7.1.2 with the green dots, meaning they land on the upper part of the first dynode. The extremely low collection efficiency of the second dynode in combination with that of the third dynode indicates that most of the particles starting from these positions on the first dynode arrive on the back of the third dynode instead of the second dynode. Additionally, a deletion process similar to that on the third dynode could be happening here as about $70\,\%$ of the particles starting from the first dynode arrive somewhere. Further investigations into this matter are necessary.

7.2 Timing parameters

The timing parameters of the PMT also show large deviations depending on the photoelectrons initial position on the photocathode. The focus of this investigation will be on the transit time (TT) of the electrons to the respective dynode stages. The results are then compared to measurement data of an mDOM PMT [22].[42]

For each initial position, the mean value of the distribution of arrival times of the electrons on the dynodes is calculated. In the previous chapter 6 the TT is obtained by fitting a Gaussian distribution to the arrival times. Since the number of electrons can be low due to the collection efficiency, the calculation of the mean value is more robust. The values between the Gaussian fit and the statistical mean are not directly comparable. However, the general shape of the TT dependence on the initial position remains similar. For the comparison to measured data, the TT obtained from the simulation is converted to the relative TT with respect to the central region of the photocathode ($r \leq 30\,\mathrm{mm}$). The result of this calculation as well as the measured data is depicted in figure 7.2.1 and figure 7.2.3 for the x- and y-direction respectively, where the blue dots correspond to the simulated data and the orange triangles to the measurement.[43]

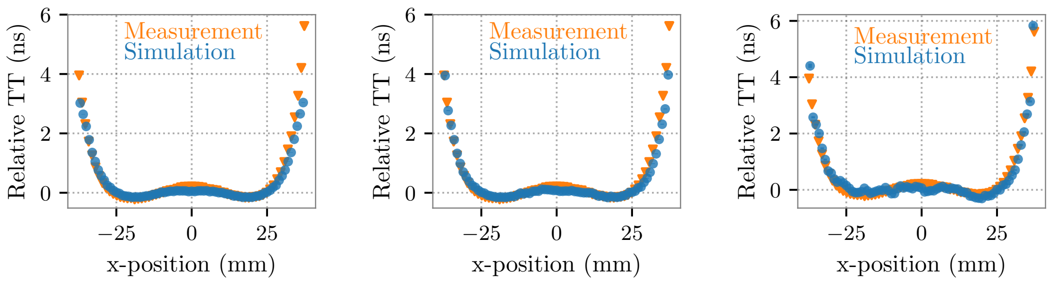

(a) First dynode **(b)** Third dynode **(c)** Anode

Figure 7.2.1: Comparison of the relative transit time of the electrons from the simulation to measurements of the mDOM PMT. The blue dots represent the simulated and the orange triangles the measured data. The measurement data is the signal at the anode which is shown for comparison in each plot. The data shows the scan of the photocathode in x-direction. Measurement data taken from [22].

The shape of the simulation results for the relative TT match those of the measurement already when considering only the arrival times at the first dynode in x-direction.[44] Generally, the measured and simulated TT increases when the edge of the PMT is illuminated. The central region is mostly flat with a slight raise in the center of the PMT ($x = 0$) which is more pronounced in the measurement than in the simulated data. After the fourth dynode the simulation data of the central region has substructures which are believed to be due to the deletion process described in section 5.5.3 and carry through to the anode (see figure 7.2.1c). The symmetry in the shape of the relative TT is expected as the geometry of the PMT is symmetric in the x-direction.

The peak to peak difference of the TT in the simulation is $(3.19 \pm 0.01)\,\mathrm{ns}$ at the first dynode and $(6.14 \pm 0.08)\,\mathrm{ns}$ at the anode. This indicates that the TT of the rest of the multiplication system does not increase uniformly. The peak to peak difference of the relative TT at the anode obtained from the simulation is larger than that of the measured data of $5.84\,\mathrm{ns}$. The difference between the used supply voltages is only $6\,\mathrm{V}$ so should not give a major contribution to this. An important note about the measurement is that it does not necessarily yield the correct value. This is due to internal reflections inside the PMT which can occur when the photon is not absorbed in the photocathode but transmitted. It can then reflect of

[42]Serial number BA0794 operated at $1206\,\mathrm{V}$.

[43]The data for dynodes not shown here can be found in figure 9.0.4 and figure 9.0.5.

[44]Keep in mind that the measured data belongs to electrons at the anode and is not available for the dynodes.

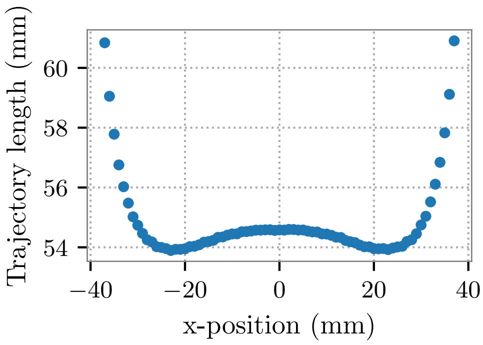

(a) Trajectory length.

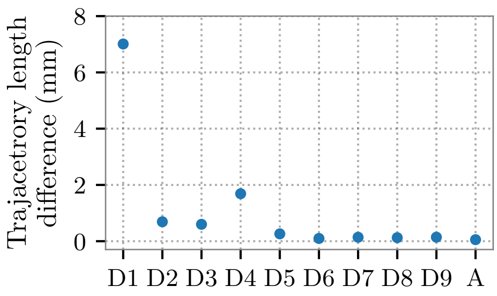

(b) Peak to peak difference.

Figure 7.2.2: Mean trajectory lengths of the electrons arriving at the first dynode along the x-direction in figure 7.2.2a. The peak to peak difference in trajectory length for each contributor of the dynode system in figure 7.2.2b.

the internal components of the PMT and be absorbed at a different position on the photocathode. Therefore, the measurement data is a convolution of multiple spots on the photocathode. This behaviour is not present in the simulation as the photoemission process in the simulation only starts with the release of an electron from the surface and does not include photon propagation.

The shape of the relative TT dependence on the initial position is caused by the different trajectory lengths between these positions. This is displayed in figure 7.2.2a for the particles arriving at the first dynode.

The shape of the mean trajectory length of the electrons propagating towards the first dynode depending on the initial position is the same as that of the TT with a peak to peak difference in trajectory length of $(7.01 \pm 0.02)\,\mathrm{mm}$. For the rest of the dynode system this value is lower as is depicted in figure 7.2.2b where the peak to peak difference of the trajectory length is presented for the multiplication system. The first dynode has the largest contribution followed by the fourth dynode with $(1.69 \pm 0.08)\,\mathrm{mm}$. The remaining dynodes are in the order of a few $0.1\,\mathrm{mm}$. This shows that the dominating contribution to the relative TT of the PMT in x-direction comes from the first multiplication stages with special emphasis on the first dynode.

In contrast to the x-direction, the geometry of the PMT is not symmetric in the y-direction. This is also represented in the measurement of the relative TT, where the TT increases for positive y-positions but decreases for negative ones. At the first dynode this behaviour is not present in the simulation data (see figure 7.2.3a) where the results and geometry of the PMT can still be considered to be symmetric around the PMT center. Better agreement between the simulation and measurement of the relative TT is found in the following dynodes with the asymmetry developing at the second dynode (see figure 7.2.3b). This is due to the differing trajectory lengths from the first to the second dynode presented in figure 7.2.4a.

The peak to peak difference between the trajectory lengths on the second dynode is $(8.37 \pm 0.02)\,\mathrm{mm}$ and caused by the emission of secondaries from different positions on the first dynode (see figure 7.1.2). The contributions from the rest of the multiplication system are depicted in figure 7.2.4b. The first dynode still has a considerable difference of $(6.06 \pm 0.03)\,\mathrm{mm}$ as expected. The datapoint for the third dynode is missing as it is biased due to the larger amount of particle hitting the back of the third dynode. As explained in

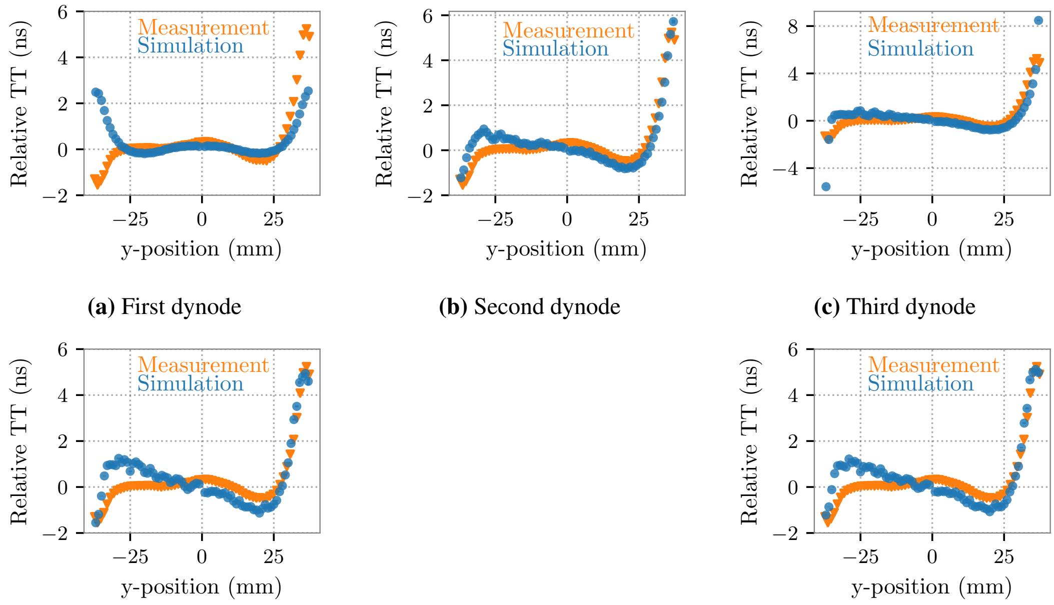

(a) First dynode **(b)** Second dynode **(c)** Third dynode

(d) Fourth dynode **(e)** Anode

Figure 7.2.3: Comparison of the relative transit time of the electrons from the simulation to measurements of the mDOM PMT. The blue dots represent the simulated and the orange triangles the measured data at the anode which is shown for comparison in each plot. The data shows the scan of the photocathode in y-direction. Measurement data taken from [22].

section 7.1, the particles emitted in $y = -37\,\mathrm{mm}$ dominantly show this behaviour and thus have a trajectory length about five times larger than expected. The fourth and fifth dynodes have larger differences compared to the x-direction of $(2.9 \pm 0.2)\,\mathrm{mm}$ and $(1.28 \pm 0.07)\,\mathrm{mm}$ respectively. An explanation for this discrepancy lies in the geometry of the PMT. Electrons emitted along the x-direction land on the first dynode with a similar spread in y-direction. This leads to the small deviation of the trajectory length between the first and second dynode for the different initial positions in x-direction on the photocathode and is mirrored for the rest of the multiplication system. If released along the y-direction, the electrons will have higher deviations in the y-positions on the first dynode as shown in figure 7.1.2. This would translate to larger deviations of the position on the second dynode which in turn widens the spread on the third dynode and so on. Thus the difference between the x- and y-direction is expected. The rest of the multiplication system again has trajectory length differences of a few $0.1\,\mathrm{mm}$ highlighting the focusing effect of the latter stages although it remains to be seen whether this holds true should proper initial conditions for the secondary particles be introduced.

The general shape of the relative TT in y-direction agrees between the simulation and measurement. However, there are some deviations between the two. The measurement data is flat for y-positions between $0\,\mathrm{mm}$ and $-30\,\mathrm{mm}$ while the simulation increases in this region. This deviation matches the behaviour of the collection efficiency presented in figure 7.1.1b for the second dynode which is due to particles hitting the back side of the third dynode. It could be possible that these particles would have a lower time of flight to the second dynode and yield a behaviour more comparable to the measurement.

The peak to peak difference of the relative TT at the anode obtained from the simulation is $(6.3 \pm 0.1)\,\mathrm{ns}$. While it does not match with that of the measurement of $6.8\,\mathrm{ns}$ the difference between the two values could be due to the contribution of internal reflections in the PMT

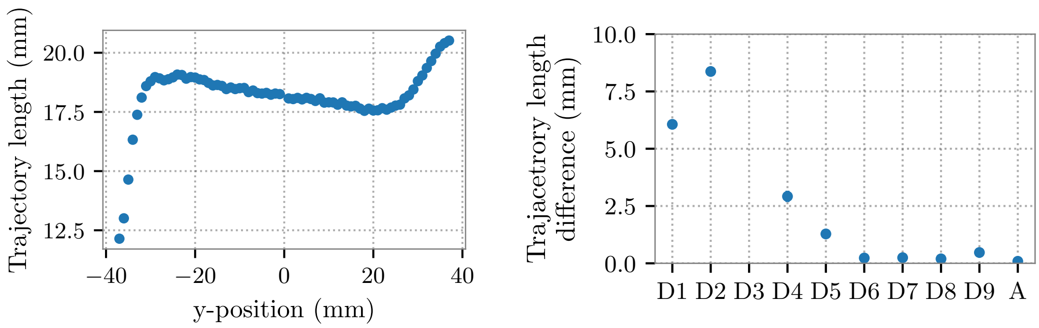

(a) Trajectory length.

(b) Peak to peak difference.

Figure 7.2.4: Trajectory lengths of the electrons arriving at the first dynode along the y-direction in figure 7.2.2a with the peak to peak difference in trajectory length for the dynode system in figure 7.2.4b.

during the measurement. A contribution due to different supply voltages is not expected the difference is only $6\,\mathrm{V}$. It is noteworthy that the peak to peak difference at the third dynode of $(14.05 \pm 0.06)\,\mathrm{ns}$ is significantly larger due to the particles originating from $y = -37\,\mathrm{nm}$ on the photocathode hitting the back of it as discussed above.

8 Summary and Outlook

The goal of this thesis is the replication of a photomultiplier in COMSOL followed by the investigation of PMT performance parameters. This is done for the PMT of one of the new modules for the IceCube Upgrade, the mDOM.

Chapter 4 outlines the first task giving a general introduction to COMSOL as well as the necessary steps in setting up the PMT simulation. The PMT geometry was obtained by CT scanning an mDOM PMT with the accuracy of the scan being in the order of a few$10\,\mu\mathrm{m}$. The photoelectrons are emitted from the photocathode with realistic initial conditions whereas those of the secondary electrons are not implemented yet. The accuracy of the simulation is investigated in chapter 5 with the final simulation conserving the energy of the particles to a point where a theoretical impact on the gain is in the sub percent region. The timing accuracy of the simulation could be improved by combining the manually created mesh with a more sophisticated choice for a constraint on the maximum time step of the solving algorithm. The latter investigation was inconclusive but indicated that the accuracy could be further improved. As the major contribution to the accuracy deficit is at the first dynode, smaller time steps around this region could be beneficial and with the correct configuration the drawback in terms of computational resources could be kept small.

The analysis of the simulated data was split into three parts corresponding to the different illumination patterns used in measurements. First, a single spot at the center of the photocathode was set to emit electrons in section 6.1 for which the collection efficiency (CE), transit time (TT) and transit time spread (TTS) are investigated. The relative CE of the multiplication system is found to be above $90\,\%$ for all dynodes except the fourth where deviations are explained with a deletion of particles in the simulation. The absolute TT of the PMT is calculated to be $(38.86 \pm 0.06)\,\mathrm{ns}$ with a TTS of $(1.36 \pm 0.06)\,\mathrm{ns}$. The latter value is larger than the TTS measured from an mDOM PMT of $(1.11 \pm 0.01)\,\mathrm{ns}$. This deviation is again explained by the deletion process which is connected to the introduction of slower moving electrons between the third and fourth dynode. These electrons are believed to be responsible for the second peak in the distribution of the arrival times. The absolute TT could not be compared to measurement as the setup in the Münster working group is not suitable for this measurement but it is comparable to the typical electron transit time given by the manufacturer of $43\,\mathrm{ns}$. The difference between the simulation result and manufacturers claim is possibly due to the $200\,\mathrm{V}$ difference in supply voltage between them. Further investigation of timing parameters depending on the wavelength of the incident photon were performed. This dependence is fitted with a linear function and while the slope of the measurement of $(-0.23 \pm 0.01)\,\mathrm{ns}/100\mathrm{nm}$ is flatter than that of the simulation data with $(-0.31 \pm 0.01)\,\mathrm{ns}/100\mathrm{nm}$, the reason behind this dependence was confirmed to be the larger spread in trajectories for smaller wavelengths. The deviations found are again explained by the deletion process and subsequent development of the second peak in arrival times.

This investigation was followed by the emission of electrons from the whole surface of the photocathode in section 6.2. The relative CE was found to be above $85\,\%$ for most of the dynode system with the deviation at the fourth dynode being due to the deletion of particles by the simulation. The shape of the arrival time distribution showed a distinct shoulder towards higher values at the first dynode. Such a shoulder is also found in PMT measurements of the anode signal when the full photocathode area is illuminated. The absolute TT in the simulation is $(39.49 \pm 0.04)\,\mathrm{ns}$ with a TTS of $(1.64 \pm 0.04)\,\mathrm{ns}$. These values are larger compared to when electrons are emitted from a central point on the photocathode as expected. The differences are explained by the larger spread in trajectories for the emission from the whole photocathode surface. Deviations between the simulation and the measurement from the Münster group as well as measurements by the manufacturer respectively are again explained by the deletion process and differences in the supply voltage.

Since the export of data from the simulation is limited in the amount of information accessible, a third analysis method is presented in chapter 7 where the positions on the photocathode surface are sampled in two directions thus emulating measurements performed to scan the photocathode for inhomogeneities. The comparison between the measurement and simulation data of the these scans showed good agreement in the x-direction, with the relative TT along this direction matching both in shape as well as magnitude. In the y-direction, however, deviations between the simulation and the measurement in negative y-direction arise. The relative TT of the measurement in this region is mostly flat while that of the simulation rises linearly. This discrepancy is possibly caused by the collection efficiency for this position. Ultimately, the shape of the relative TT of measurement and simulation is similar with minor deviations and the absolute values are matching, leading again to an agreement between simulation and measurement. One benefit of the simulation considering this investigation is that there is no internal reflection present. This can occur when the photon is not absorbed but transmitted through the photocathode and then reflected of the internal structure of the PMT only to be absorbed at a different position. This results in a convolution of the position in the measurement and could account for differences between the simulation and measurement results.

Further studies with COMSOL can be done for any PMT property. It has been shown that the properties of the photomultiplier strongly depend on the magnetic field [22]. This poses several problems for the deployment of the mDOM, since the final orientation in the ice is not known before the deployment. It is also possible to implement this feature in COMSOL by using the *magnetic force* domain property. Additionally, the performed scans could be extended to the whole surface instead of only two directions in combination with wavelength and magnetic field dependent studies for each position. Improvements of the simulation accuracy as well as the implementation of more PMT features like different pulse types and proper secondary emission are also possible.

In summary, in this work a simulation has been created which can still be extended but already reproduces properties of a PMT both qualitatively and quantitatively.

9 Appendix

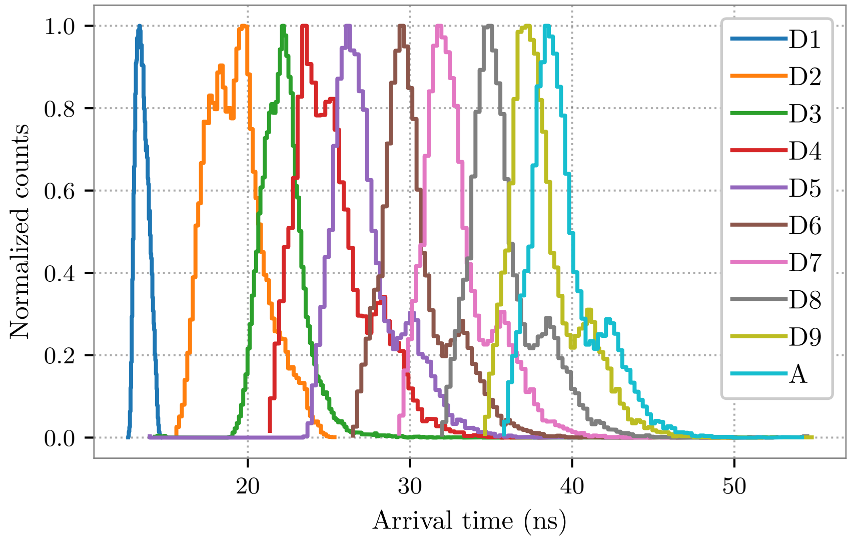

Figure 9.0.1: Distribution of the arrival times of the electrons at the different multiplication stages for the emission of electrons from a central spot on the photocathode.

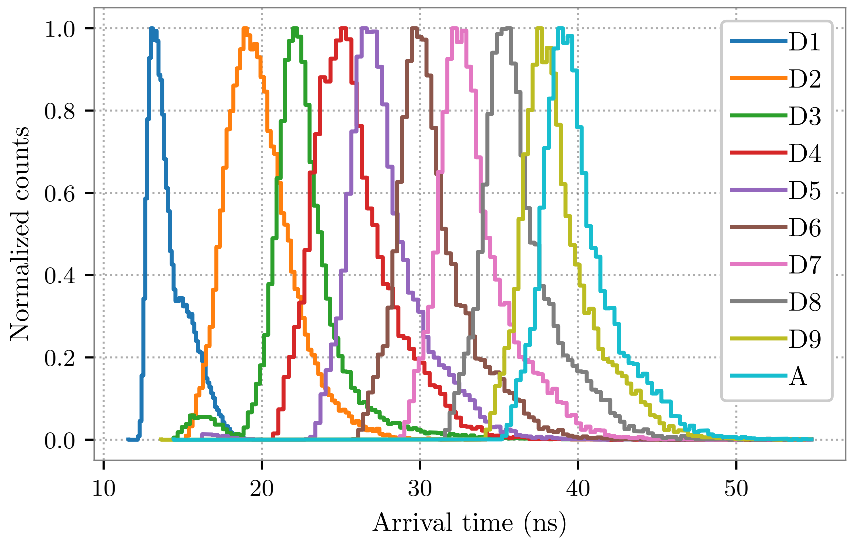

Figure 9.0.2: Distribution of the arrival times of the electrons at the different multiplication stages for the emission of electrons from the whole photocathode surface.

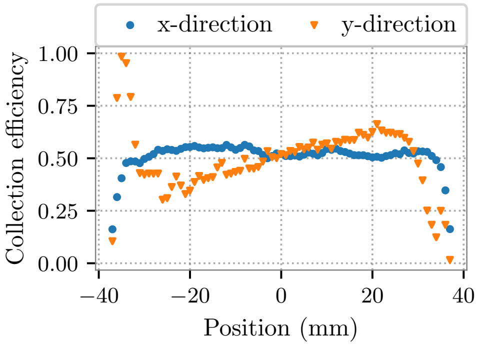

(a) Fifth dynode

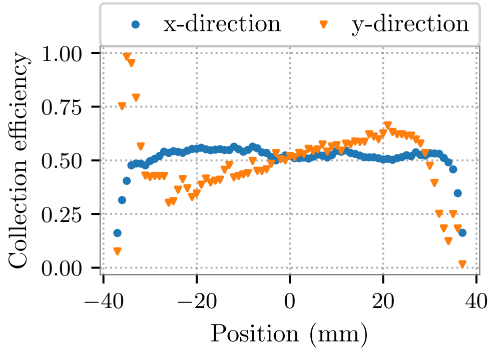

(b) Sixth dynode

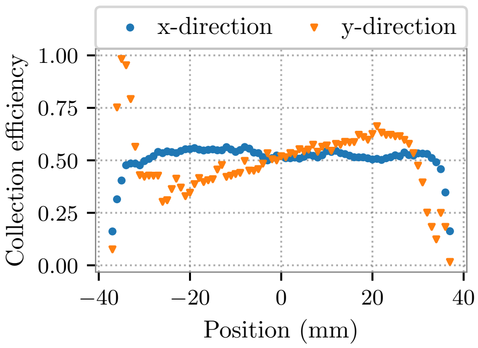

(c) Seventh dynode

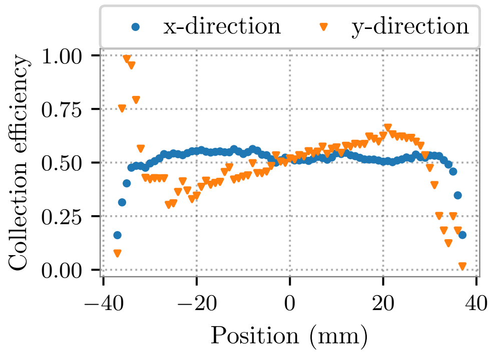

(d) Eighth dynode

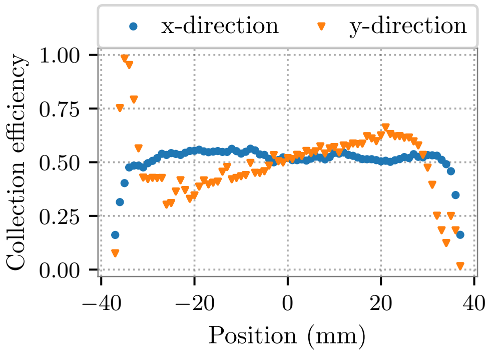

(e) Ninth dynode

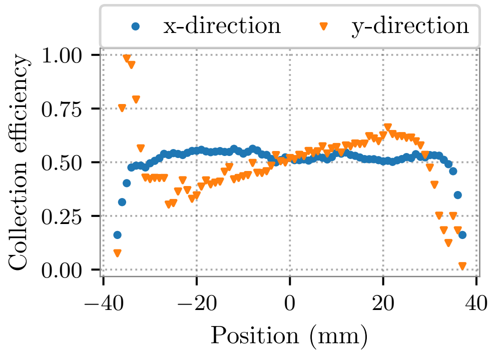

(f) Anode

Figure 9.0.3: Collection efficiency of the PMT along the x- (blue dots) and y-axis (orange triangles) with respect to the number of emitted photoelectrons.

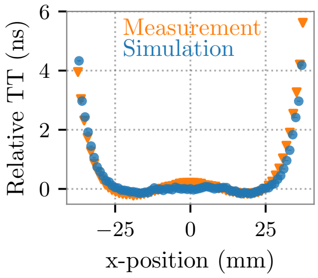

(a) Second dynode.

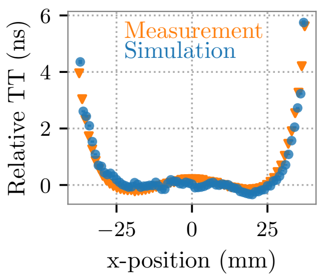

(b) Fourth dynode.

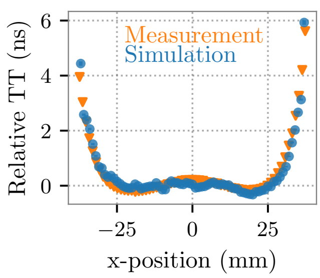

(c) Fifth dynode.

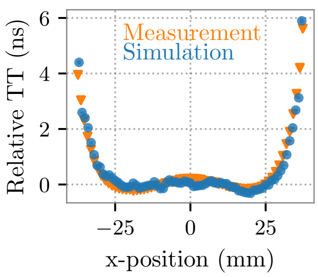

(d) Sixth dynode.

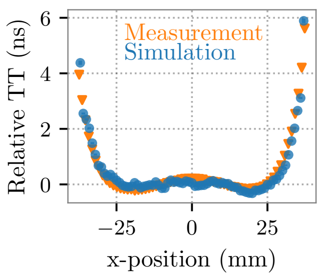

(e) Seventh dynode.

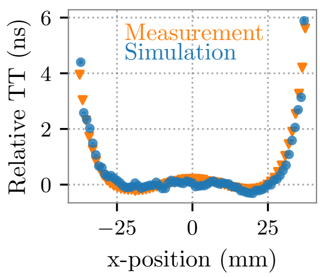

(f) Eighth dynode.

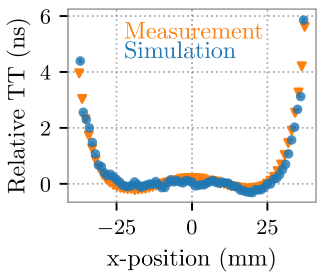

(g) Ninth dynode.

Figure 9.0.4: Relative transit time of the electrons from the simulation and measurement of the mDOM PMT in x-direction. The blue dots correspond to the simulation and the orange triangles to the measurement. Measurement data taken from [22].

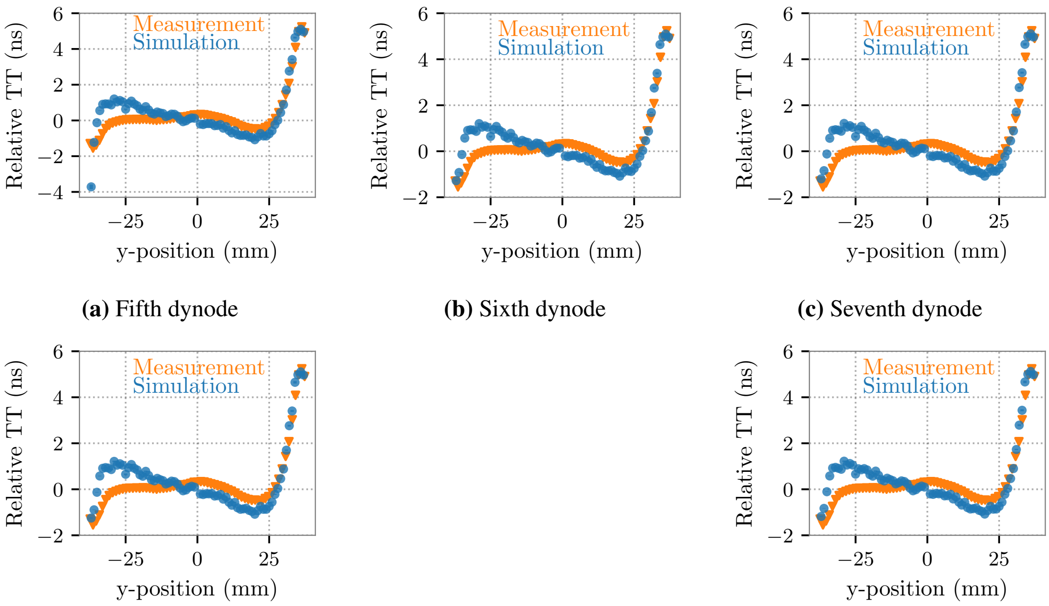

(a) Fifth dynode

(b) Sixth dynode

(c) Seventh dynode

(d) Eighth dynode

(e) Ninth dynode

Figure 9.0.5: Relative transit time of the electrons from the simulation and measurement of the mDOM PMT in y-direction. The blue dots correspond to the simulation and the orange triangles to the measurement. Measurement data taken from [22].

Bibliography

[1] Rudolf L. Mößbauer. *History of Neutrino Physics Pauli's Letters*. 2014. URL: https://web.archive.org/web/20140520221117/http://www.neutrino.uni-hamburg.de/sites/site_neutrino/content/e45939/e48540/e48541/e48544/infoboxContent48545/material-vorlesung1-moessbauer-pauli.pdf (visited on 07/13/2023).

[2] C. L. Cowan et al. "Detection of the Free Neutrino: a Confirmation". In: *Science* 124.3212 (1956), pp. 103–104. DOI: 10.1126/science.124.3212.103. eprint: https://www.science.org/doi/pdf/10.1126/science.124.3212.103. URL: https://www.science.org/doi/abs/10.1126/science.124.3212.103.

[3] Francis Halzen and Spencer R. Klein. "Invited Review Article: IceCube: An instrument for neutrino astronomy". en. In: *Review of Scientific Instruments* 81.8 (2010). DOI: 10.1063/1.3480478. URL: http://dx.doi.org/10.1063/1.3480478.

[4] P. A. Cerenkov. "Visible Radiation Produced by Electrons Moving in a Medium with Velocities Exceeding that of Light". In: *Phys. Rev.* 52 (4 Aug. 1937), pp. 378–379. DOI: 10.1103/PhysRev.52.378. URL: https://link.aps.org/doi/10.1103/PhysRev.52.378.

[5] Aya Ishihara. *The IceCube Upgrade – Design and Science Goals*. 2019. arXiv: 1908.09441 [astro-ph.HE].

[6] M G Aartsen et al. "IceCube-Gen2: the window to the extreme Universe". In: *Journal of Physics G: Nuclear and Particle Physics* 48.6 (2021), p. 060501. DOI: 10.1088/1361-6471/abbd48.

[7] Nasfarley88 MissMJ. 2014. URL: https://commons.wikimedia.org/wiki/File:Standard_Model_of_Elementary_Particles_modified_version.svg (visited on 04/19/2023).

[8] Y. Fukuda et al. "Evidence for Oscillation of Atmospheric Neutrinos". In: *Phys. Rev. Lett.* 81 (8 1998), pp. 1562–1567. DOI: 10.1103/PhysRevLett.81.1562. URL: https://link.aps.org/doi/10.1103/PhysRevLett.81.1562.

[9] The KATRIN collaboration et al. "The design, construction, and commissioning of the KATRIN experiment". In: *Journal of Instrumentation* 16.08 (2021), T08015. DOI: 10.1088/1748-0221/16/08/T08015. URL: https://dx.doi.org/10.1088/1748-0221/16/08/T08015.

[10] M. Aker et al. "Direct neutrino-mass measurement with sub-electronvolt sensitivity". en. In: 18 (2022), 160–166. DOI: 10.1038/s41567-021-01463-1. URL: http://dx.doi.org/10.1038/s41567-021-01463-1.

[11] T. K. Gaisser, T. Stanev, and S. Tilav. "Cosmic Ray Energy Spectrum from measurements of Air Showers". In: *Frontiers of Physics* 8.6 (2013), 748–758. DOI: 10.1007/s11467-013-0319-7.

[12] Christian Spiering. “Towards high-energy neutrino astronomy”. In: *The European Physical Journal H* 37.3 (2012), 515–565. DOI: `10.1140/epjh/e2012-30014-2`.

[13] The IceCube Collaboration et al. “Multimessenger observations of a flaring blazar coincident with high-energy neutrino IceCube-170922A”. In: *Science* 361.6398 (2018), eaat1378. DOI: `10.1126/science.aat1378`. eprint: `https://www.science.org/doi/pdf/10.1126/science.aat1378`. URL: `https://www.science.org/doi/abs/10.1126/science.aat1378`.

[14] IceCube Collaboration et al. “Neutrino emission from the direction of the blazar TXS 0506+056 prior to the IceCube-170922A alert”. In: *Science* 361.6398 (2018), pp. 147–151. DOI: `10.1126/science.aat2890`. eprint: `https://www.science.org/doi/pdf/10.1126/science.aat2890`. URL: `https://www.science.org/doi/abs/10.1126/science.aat2890`.

[15] R. Abbasi et al. “Evidence for neutrino emission from the nearby active galaxy NGC 1068”. In: *Science* 378.6619 (Nov. 2022), pp. 538–543. DOI: `10.1126/science.abg3395`.

[16] IceCube Collaboration et al. “Observation of high-energy neutrinos from the Galactic plane”. In: *Science* 380.6652 (2023), pp. 1338–1343. DOI: `10.1126/science.adc9818`. eprint: `https://www.science.org/doi/pdf/10.1126/science.adc9818`. URL: `https://www.science.org/doi/abs/10.1126/science.adc9818`.

[17] Arpad Horvath. 2006. URL: `https://en.wikipedia.org/wiki/File:Cherenkov.svg` (visited on 04/20/2023).

[18] M.G. Aartsen et al. “The IceCube Neutrino Observatory: instrumentation and online systems”. In: *Journal of Instrumentation* 12.03 (Mar. 2017), P03012–P03012. DOI: `10.1088/1748-0221/12/03/p03012`.

[19] IceCube Masterclass. 2023. URL: `https://masterclass.icecube.wisc.edu/en/learn/detecting-neutrinos` (visited on 04/25/2023).

[20] R. Abbasi et al. “A muon-track reconstruction exploiting stochastic losses for large-scale Cherenkov detectors”. In: *Journal of Instrumentation* 16.08 (2021), P08034. DOI: `10.1088/1748-0221/16/08/P08034`. URL: `https://dx.doi.org/10.1088/1748-0221/16/08/P08034`.

[21] M G Aartsen et al. “IceCube-Gen2: the window to the extreme Universe”. In: *Journal of Physics G: Nuclear and Particle Physics* 48.6 (Apr. 2021), p. 060501. DOI: `10.1088/1361-6471/abbd48`. URL: `https://dx.doi.org/10.1088/1361-6471/abbd48`.

[22] Martin Antonio Unland Elorrieta. “Development, simulation, and characterisation of a novel multi-PMT optical module for IceCube Upgrade with emphasis on detailed understanding of photomultiplier performance parameters”. PhD thesis. Westfälische Wilhelms-Universität Münster, 2023. URL: `https://zenodo.org/record/8121321` (visited on 07/13/2023).

[23] Martin Antonio Unland Elorrieta. “Studies on dark rates induced by radioactive decays of the multi-PMT digital optical module for future IceCube extensions”. Master thesis. Westfälische Wilhelms-Universität Münster, 2017. URL: `https://www.uni-muenster.de/imperia/md/content/physik_kp/agkappes/abschlussarbeiten/masterarbeiten/1712-ma_munland.pdf` (visited on 05/05/2023).

[24] Markus Dittmer. "Characterisation of scintillation light induced by radioactive excitation in the mDOM glass pressure vessel". Master thesis. Westfälische Wilhelms-Universität Münster, 2020. URL: https://www.uni-muenster.de/imperia/md/content/physik_kp/agkappes/abschlussarbeiten/masterarbeiten/dittmer.pdf (visited on 05/05/2023).

[25] Hamamatsu Photonics K.K. *Photomultiplier Tube R12199*. 2015. URL: https://hamamatsu.su/files/uploads/pdf/1_%D1%84%D1%8D%D1%83_%D0%B8_%D0%BC%D0%BE%D0%B4%D1%83%D0%BB%D0%B8/%D1%81%D0%BF%D0%B5%D0%BA%D1%82%D1%80%D0%BE%D0%BC%D0%B5%D1%82%D1%80%D0%B8%D1%87%D0%B5%D1%81%D0%BA%D0%B8%D0%B5_%D1%84%D1%8D%D1%83/%D1%81%D0%BF%D0%B5%D1%86%D1%84%D0%BE%D1%80%D0%BC%D0%B0/r12199_tpmh1356e.pdf (visited on 06/12/2023).

[26] W. E. Spicer. "Photoemissive, Photoconductive, and Optical Absorption Studies of Alkali-Antimony Compounds". In: *Phys. Rev.* 112 (1 Oct. 1958), pp. 114–122. DOI: 10.1103/PhysRev.112.114. URL: https://link.aps.org/doi/10.1103/PhysRev.112.114 (visited on 04/26/2023).

[27] John Smedley. "Cathode Physics". 2012. URL: https://uspas.fnal.gov/materials/12UTA/Lecture1.pdf (visited on 04/26/2023).

[28] Carl Hepburn. *Basic Semiconductor Physics, Britney Spears' Guide to Semiconductor Physics*. 2000. URL: http://britneyspears.ac/physics/basics/basics.htm (visited on 04/27/2023).

[29] S-O Flyckt and Carole Mamonier. *Photomultiplier tubes: principles & applications*. Photonis, 2002.

[30] Hamamatsu Photonics K.K. *Photomultiplier Tubes - Basics and Applications 4th edition*. 2017. URL: https://www.hamamatsu.com/content/dam/hamamatsu-photonics/sites/documents/99_SALES_LIBRARY/etd/PMT_handbook_v4E.pdf (visited on 05/03/2023).

[31] A. G. Wright. *The Photomultiplier Handbook*. Oxford University Press, June 2017. ISBN: 9780199565092. DOI: 10.1093/oso/9780199565092.001.0001. URL: https://doi.org/10.1093/oso/9780199565092.001.0001.

[32] COMSOL Multiphysics. *The Finite Element Method (FEM)*. 2017. URL: https://www.comsol.com/multiphysics/finite-element-method?parent=physics-pdes-numerical-042-62 (visited on 05/04/2023).

[33] COMSOL Multiphysics. *COMSOL Documentation*. 2023. URL: https://doc.comsol.com/6.1/docserver/#!/com.comsol.help.comsol/helpdesk/helpdesk.html (visited on 05/08/2023).

[34] ZEISS Deutschland. *ZEISS Quality Excellence Center Messtechnische Dienstleistungen in Köln*. 2023. URL: https://www.zeiss.de/messtechnik/services-und-support/standorte/koeln.html (visited on 05/08/2023).

[35] Kevin Gräve. private communication. 2022.

[36] Autodesk Inc. *Autodesk Inventor: Mechanische Konstruktionssoftware für anspruchsvolle Ideen*. 2023. URL: https://www.autodesk.de/products/inventor/overview?term=1-YEAR&tab=subscription (visited on 07/06/2023).

[37] Fynn Peters. “Studien zur Wellenlängenabhängigkeit von Performance-Parametern von Photomultipliern des Typs Hamamatsu R12199-01HA”. Bachelor thesis. Westfälische Wilhelms-Universität Münster, 2020. URL: `https://www.uni-muenster.de/imperia/md/content/physik_kp/agkappes/abschlussarbeiten/bachelorarbeiten/ba_fpeters.pdf` (visited on 05/08/2023).

[38] R. Nathan and C. H. B. Mee. “The energy distribution of photoelectrons from the K2CsSb photocathode”. In: *physica status solidi (a)* 2.1 (1970), pp. 67–72. DOI: `https://doi.org/10.1002/pssa.19700020107`. eprint: `https://onlinelibrary.wiley.com/doi/pdf/10.1002/pssa.19700020107`. URL: `https://onlinelibrary.wiley.com/doi/abs/10.1002/pssa.19700020107`.

[39] Chunghsin Lee. “Photoelectron energy distribution of Cs3Sb”. In: *Journal of Applied Physics* 54.8 (Aug. 1983), pp. 4578–4580. ISSN: 0021-8979. DOI: `10.1063/1.332659`. eprint: `https://pubs.aip.org/aip/jap/article-pdf/54/8/4578/7980068/4578\_1\_online.pdf`. URL: `https://doi.org/10.1063/1.332659`.

[40] Prof. Dr. Helmut Zacharias. private communication. 2023.

[41] Matthew Newville et al. *LMFIT: Non-Linear Least-Square Minimization and Curve-Fitting for Python*. Version 0.8.0. Sept. 2014. DOI: `10.5281/zenodo.11813`. URL: `https://doi.org/10.5281/zenodo.11813`.

[42] Christopher Boucher. *Sampling Random Numbers from Probability Distribution Functions*. 2016. URL: `https://www.comsol.de/blogs/sampling-random-numbers-from-probability-distribution-functions/` (visited on 05/09/2023).

[43] Emmanuel Agullo et al. *MUMPS: MUltifrontal Massively Parallel sparse direct Solver*. 2023. URL: `https://mumps-solver.org/index.php` (visited on 05/11/2023).

[44] Youcef Saad and Martin H. Schultz. “GMRES: A Generalized Minimal Residual Algorithm for Solving Nonsymmetric Linear Systems”. In: *SIAM Journal on Scientific and Statistical Computing* 7.3 (1986), pp. 856–869. DOI: `10.1137/0907058`. eprint: `https://doi.org/10.1137/0907058`. URL: `https://doi.org/10.1137/0907058`.

[45] J. Chung and G. M. Hulbert. “A Time Integration Algorithm for Structural Dynamics With Improved Numerical Dissipation: The Generalized-alpha Method”. en. In: *Journal of Applied Mechanics* 60.2 (June 1993), 371–375. DOI: `10.1115/1.2900803`. URL: `http://dx.doi.org/10.1115/1.2900803`.

[46] Jan-Philipp Weiss. *Automatic Time Step and Order Selection in Time-Dependent Problems*. 2019. URL: `https://www.comsol.com/blogs/automatic-time-step-and-order-selection-in-time-dependent-problems/`.

[47] COMSOL Multiphysics support. private communication. 2022.

[48] Walther Frei. *How Large of a Model Can You Solve with COMSOL®?* 2022. URL: `https://www.comsol.de/blogs/much-memory-needed-solve-large-comsol-models/` (visited on 05/10/2023).

[49] Saskia Schmiemann. “Squark Annihilation Contributions to Neutralino Dark Matter in NLO SUSY-QCD”. PhD thesis. Westfälische Wilhelms-Universität Münster, 2019. URL: `https://www.uni-muenster.de/imperia/md/content/physik_tp/theses/klasen/schmiemann_phd.pdf` (visited on 05/05/2023).

[50] Janis Averbeck. "Nachbau eines Photomultipliers in COMSOL Multiphysics® und Untersuchung der Elektronentrajektorien zwischen Photokathode und erster Dynode". Bachelor thesis. Westfälische Wilhelms-Universität Münster, 2022. URL: https://www.uni-muenster.de/imperia/md/content/physik_kp/agkappes/abschlussarbeiten/bachelorarbeiten/bachelor_janis.pdf (visited on 05/05/2023).

[51] John Hennig et al. "MPh-py/MPh: 1.2.3". In: (2023). DOI: 10.5281/zenodo.7749502.

[52] E.H. Bellamy et al. "Absolute calibration and monitoring of a spectrometric channel using a photomultiplier". In: *Nuclear Instruments and Methods in Physics Research Section A: Accelerators, Spectrometers, Detectors and Associated Equipment* 339.3 (1994), pp. 468–476. ISSN: 0168-9002. DOI: https://doi.org/10.1016/0168-9002(94)90183-X. URL: https://www.sciencedirect.com/science/article/pii/016890029490183X.

Declaration of Academic Integrity

I hereby confirm that this thesis on the “Replication of a photomultiplier in COMSOL Multiphysics® to study PMT performance parameters for the mDOM in IceCube” is solely my own work and that I have used no sources or aids other than the ones stated. All passages in my thesis for which other sources, including electronic media, have been used, be it direct quotes or content references, have been acknowledged as such and the sources cited.

Münster, Monday 18th September, 2023:

I agree to have my thesis checked in order to rule out potential similarities with other works and to have my thesis stored in a database for this purpose.

Münster, Monday 18th September, 2023:

Acknowledgement

I would like to express my gratitude to Alexander Kappes for providing me with the opportunity to write this thesis in his working group as well as Christian Weinheimer for volunteering as the second examiner.

A big shoutout goes to the whole working group, not only for the constant support while doing the thesis but also the engaging talks during lunch. Especially noteworthy are the guys from room 225 who I could always ask questions and present my problems to find solutions. I am grateful to everyone that took the time to proofread this thesis and helped transform it into something readable.

A big thank you also goes to the friends I made along my academic way. I am not sure that I would have made my way though physics without the engaging discussions we had and the combined struggle with some of the problem sheets.

Lastly, I want to thank my family who also supported me through my whole studies here at the university of Münster. Without my parents who provided me with this opportunity it would not have been possible.